Review Article

Static softening behavior of 316L stainless steel under flexible rolling process

Caiyi Liu [a,**], Shicheng Liang [a], Shuo Guo [a], Ruowei Li [a], Silvia Barella [b], Yan Peng [a,*], Andrea Gruttadauria [b], Marco Belfi [b], Wei Li [c], Chang Yuan [a,d], Carlo Mapelli [b]

[a] National Engineering Research Center for Equipment and Technology of Cold Strip Rolling, Yanshan University, Qinhuangdao, 066004, China
[b] Department of Mechanical Engineering, Politecnico di Milano, Milan, 20156, Italy
[c] WISDRI Engineering & Research Incorporation Limited, Wuhan 430223, China
[d] School of Mathematics, University of Bristol, Bristol, BS8 1QU, UK

ARTICLE INFO

ABSTRACT

Flexible rolling is important for increasing rolling production capacity. Since the wear rolls withdrawn and new rolls launched into the rolling process causing thermal deformation parameters variation, such as deformation temperature, strain rate, and strain. This paper studies the coupling behavior of static recrystallization (SRX), metadynamic recrystallization (MDRX), and thermal deformation parameters based on the double-pass thermal simulation experiments, analyzes the flow stress curves and reveals the variation law of recrystallization with thermal deformation parameters. The result shows that the second-pass flow stress of SRX is significantly dependent on the inter-pass time, deformation temperature and strain rate, Compared to MDRX, SRX requires time to nucleus of conception and is more influenced by initial strain. Considering the recovery effect and the multi-pass static softening solution algorithm of materials, the kinetic models of SRX and MDRX are established, and the predicted values of the models are in good agreement with the experimental values. The EBSD microstructure characterization technique is used to characterize the morphology of SRX and MDRX. The result shows that increasing inter-pass time, deformation temperature and strain rate can promote the SRX and MDRX process and improve static softening effect. Under the condition of constant deformation temperature and strain rate, increasing the initial strain can increase the SRX volume fraction. However, deformation temperature and strain rate have a more significant effect on the static softening than the initial strain. This paper provides a theoretical basis for designing and optimizing recrystallization behavior of flexible rolling gaps.

---

 * Corresponding author.
 ** Corresponding author.
   E-mail addresses: liucaiyi@ysu.edu.cn (C. Liu), pengyan@ysu.edu.cn (Y. Peng).

1.　Introduction

During the conventional rolling process, the production line is forced to stop due to roll wear and replace the rolls. Flexible rolling is an advanced manufacturing and forming technology that enables continuous rolling to increase production capacity by wear rolls withdrawn and new rolls are launched into the rolling process to complete online roll changes [1–3]. During this period, the previous thermal deformation of the sub-structure in a thermodynamically unstable state, the microstructure will change significantly between passes, with the reduction of deformation resistance gradually slowing down the effects of work hardening to achieve a stable state. This softening behavior that occurs between multiple passes of thermal deformation is called static softening, mainly including: static reversion (SRV) [4], static recrystallization (SRX) [5] and metadynamic recrystallization (MDRX) [6]. SRX and MDRX are the main forms of static softening between passes due to the difficulty of stainless steel dislocation cross-slip movement and the weak role of SRV between passes [7,8].

Dong et al. studied the static softening behavior of SA508-III steel by Gleeble1500D double-pass thermal compression experiment and analyzed the influence of different initial heating temperature, strain rate and inter-pass time on the static softening of the material. The results showed that the static softening was greatly affected by strain rate, deformation temperature, and less by strain [9,10]. Lin et al. studied similar conclusions by studying 42CrMo steel. The results showed that the volume fraction of MDRX gradually increased with the increase of strain rate and deformation temperature, and the initial strain had less influence on MDRX, and accordingly established a MDRX kinetic model that can be embedded in the simulation analysis [11]. Lin et al. studied that the volume fraction of nickel-based alloys could not be determined by the conventional four methods for calculating the MDRX volume fraction (the compensation method [12,13], the post-interpolation method [14], the average stress method [15] and the 5% total strain method [16]). A new method (maximum stress method) was proposed to calculate the MDRX volume fraction of nickel-based alloys. The MDRX behavior of materials under thermal deformation is analyzed, and the results showed that the MDRX volume fraction increases with the increase of deformation temperature, strain rate and inter-pass time [17]. Lin et al. studied the MDRX behavior of 2124 aluminum alloy and proposed a peak stress method to calculate the MDRX volume fraction, which showed that the predicted value calculated by this method was consistent with the experimental value, and could be used to predict the MDRX volume fraction in the thermal deformation process of aluminum alloy [18]. Maghsoudi et al. studied the double-pass thermal deformation high-temperature flow behavior of magnesium alloys, and characterized the formed organization with the help of optical microscopy. The results showed that the occurrence of MDRX leads to an increase in the work hardening rate and flow stress in the subsequent deformation process, which affects the DRX behavior of the second-pass [19]. Razali et al. studied that the static recrystallization behavior of 42CrMo steel by non-isothermal hot compression tests and embedded the developed SRX kinetic model into finite element software for visualization. The results show that the microstructure evolution during SRX is mainly influenced by temperature, strain rate, degree of deformation and initial austenite in terms of grain size [20]. The above studies mainly analyze the influence of different material types and thermal deformation conditions (inter-pass time, deformation temperature, strain rate and other parameters) on the macroscopic flow behavior and microstructure evolution of materials, and simulates the conventional rolling forming process through the physical simulation platform to analyze the influence on the microstructure of materials under different deformation temperature and strain rate.

Due to the continuous change of the strip thickness in the rolling direction during flexible rolling, the influence of the coupling interaction of deformation, temperature and speed on the static softening behavior of materials during the high-temperature plastic deformation process is more complex, so it is necessary to conduct a comprehensive and systematic study on the SRX and MDRX behaviors during coupled changes in flexible rolling deformation parameters.

The existing research mainly focuses on the influence of deformation temperature and strain rate on the recrystallization behavior, while the research on strain focuses on whether the strain reaches the critical strain of DRX, without sufficiently considering the relationship between the macroscopic flow behavior, microstructure evolution law of materials and the behavior of SRX and MDRX under different deformation states. Therefore, it is still necessary to conduct comprehensive studies on SRX, MDRX flow behavior and microstructure evolution mechanism.

2.　Materials and methods

2.1.　Experimental materials

In this paper, ASTM-316L hot-rolled strip is selected to study the static softening behavior of the thermal deformation process. Its chemical composition is measured by carbon/sulfur analyzer and X-ray fluorescence spectrometer, as shown in Table 1. Since the high-temperature austenite microstructure of the selected material can be stably preserved to room temperature during plastic deformation, interference with the representation of the original austenite microstructure by phase transition similar to the high-temperature quenching process of plain carbon steel is avoided [21–23]. This facilitates an in-depth study of the SRX and MDRX behavior of the materials under the change of various thermal deformation parameters.

2.2.　Experimental details

In this paper, the Gleeble 3800-GTC thermomechanical simulation experimental machine is applied to study the stress–strain relationship during the double-pass thermal deformation of the material using the equivalent substitution method, and the research method is shown in Fig. 1. Firstly, the original strip is machined into a cylindrical sample of φ8 mm $\times$ 12 mm along the thickness direction, and the test

Table 1 — Chemical composition of the ASTM-316L steel (wt.%).

C	Si	Cr	Mn	P	S	Ni	Mo	N	Fe
0.022	0.59	16.7	1.49	0.026	0.001	10.13	2.05	0.035	Bal.
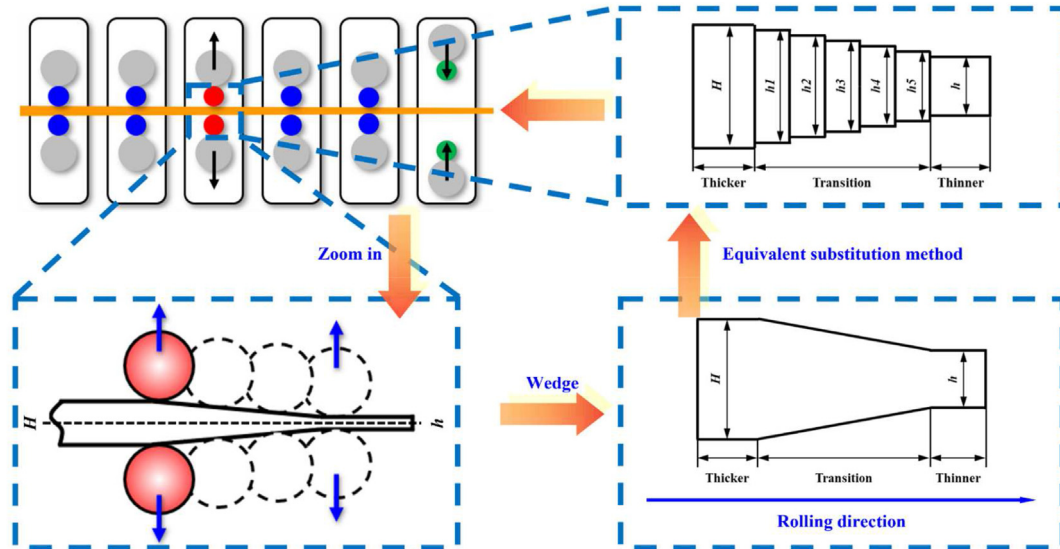
Fig. 1 — Research methodology used in this paper.

system automatically records the stress—strain data during the thermal deformation process of the material. To improve the stability and uniformity of the deformation process, a tantalum sheet with a thickness of 0.1 mm is placed between the two sides of the cylindrical sample and the indenter to prevent the sample from diffusion bonding or interfacial melting and adhesion to the indenter during high-temperature deformation. The graphite sheet is cut into discs with diameters 1.5 mm—2 mm larger than the diameter of the sample and arranged between the indenter and the sample to increase the resistor at the interface to ensure uniform temperature in the axial direction of the sample. The K-type thermocouple is welded to the axial center of the sample to record the temperature change pattern of the sample during the experiment.

The steel is subjected to double-pass thermal compression experiments, and the specific experimental scheme is shown in Fig. 2. The samples are heated to 1150 °C at a heating rate of 10 °C/s before deformation, held for 240 s to homogenize the austenite organization, followed by a cooling rate of 5 °C/s to 950 °C, 1000 °C, 1050 °C, 1100 °C, and again held for 60 s to reduce the temperature gradient during deformation. The strain rates are set to 0.01 s^{-1}, 0.1 s^{-1} and 1 s^{-1}, pre-strains are set to 0.1, 0.15, 0.2, 0.4, 0.5 and 0.6, and inter-pass times are 1 s, 10 s, 30 s and 100 s, respectively. The samples are subjected to the following two elements at the end of the holding period: (a) the samples are quenched directly after temperature preservation in the deformation gap to study the effect of different thermal deformation processes on the microstructure, (b) the samples are subjected to the second thermal compression deformation with the same deformation parameters as the first-pass, which is used to construct the

kinetic models of SRX and MDRX and calculate the degree of SRX and MDRX softening.

After the double-pass thermal compression experiments, the samples are quickly quenched to room temperature in order to preserve the high-temperature microstructure. The quenched samples are precisely split along the axial direction of the contact surface with the indenter using a Micracut 202 precision cutter, and the center of the split surface is preferentially selected for organization characterization. The samples are inlaid, ground, mechanically polished and electrolytically polished with 6% perchloric acid +94% acetic acid solution at 40 V, electrolysis time of 15—20 s, current of 0.2—0.7 A, and electrolysis temperature of 22 °C. The EBSD characterization is carried out with a Zeiss Sigma 500 SEM (Scanning Electron Microscope) equipped with an Oxford C-Nano detector. This study defines grain orientations in the range of 2—15° to be small angle grain boundaries above 15° to be large angle grain boundaries [3].

3. Results and discussion

3.1. Kinetics analysis

3.1.1. Flow stress curve of SRX
The flow stress curves obtained for the experimental steel in the coupled state of inter-pass time, deformation temperature, strain rate and pre-strain are shown in Fig. 3. It can be seen from the figure that in the double-pass thermal compression process, the first-pass yield stress is less than the second-pass yield stress, and the increasing trend of the second-pass flow stress is always less than the epitaxial curve
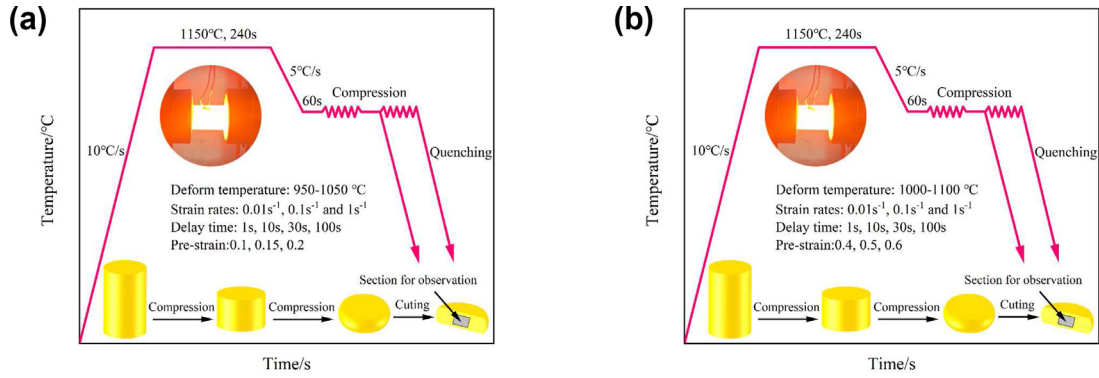
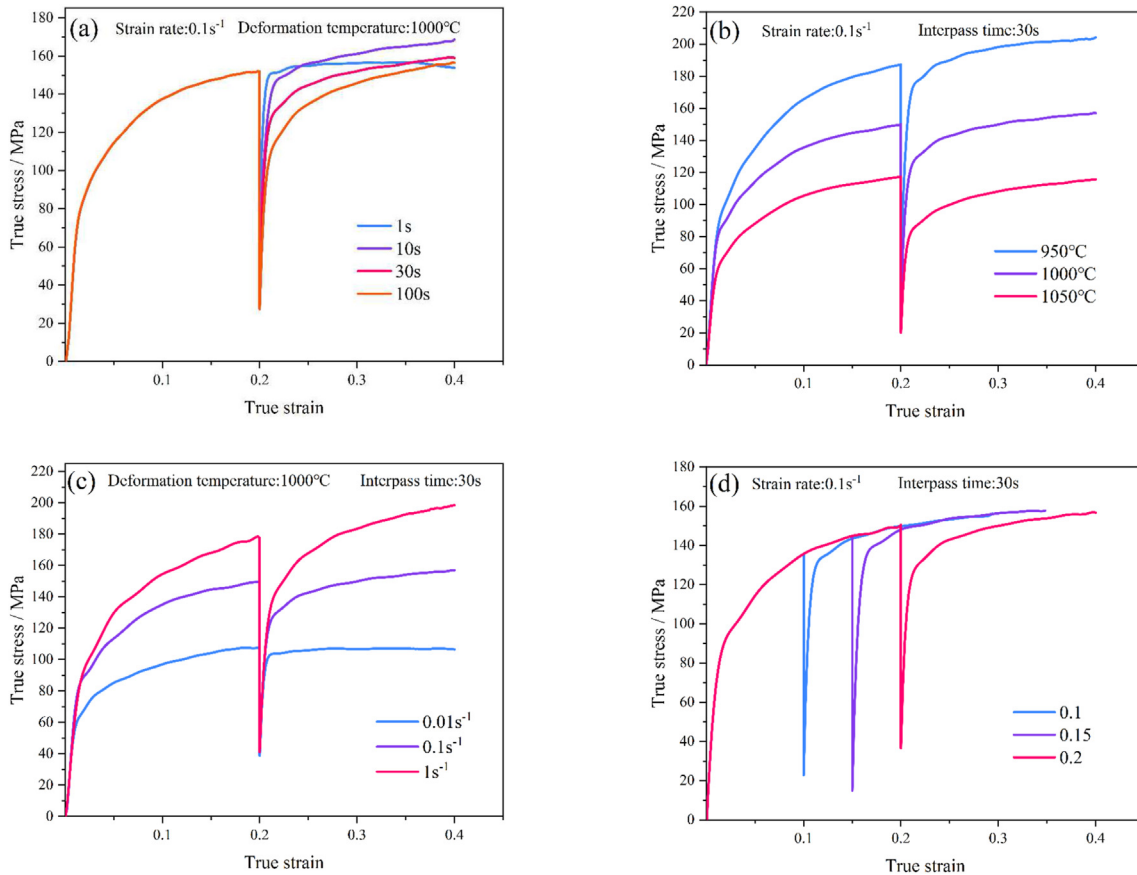Fig. 2 – Experimental procedure. (a) SRX experiment, (b) MDRX experiment.

Fig. 3 – The static recrystallization flow stress curves of the experimental steel by double-pass thermal compression tests. (a) Inter-pass times, (b) deformation temperatures, (c) strain rates, (d) pre-strains.

of the first-pass flow stress in most thermal deformation states [24,25]. The reason for this phenomenon is that the flow stress increases with increasing dislocation density in the first stage under the effect of work hardening, and the reversion and recrystallization behavior occurs in the subsequent inter-pass, reducing the dislocation density inside the grains. As the degree of deformation in the first-pass does not reach the critical condition for the occurrence of DRX, it indicates that the SRX process is occurring in the inter-pass [26,27]. Fig. 3(a) shows the flow stress curves under different inter-pass times. It can be seen that the second-pass flow stress decreases with

increasing inter-pass time, indicating that the rate of softening of the material by SRX increases with increasing inter-pass time. When inter-pass time is 100 s, the second-pass yield stress is closer to the first-pass yield stress, and the dislocations are further eliminated indicating that the SRX process needs time to nucleation. The longer the inter-pass time, the more fully SRX is carried out and the more favorable the softening effect of SRX. Fig. 3(b) shows the flow stress curves under different deformation temperatures. It can be seen that as deformation temperature continues to rise, the flow stress in the first and second passes gradually decreases.
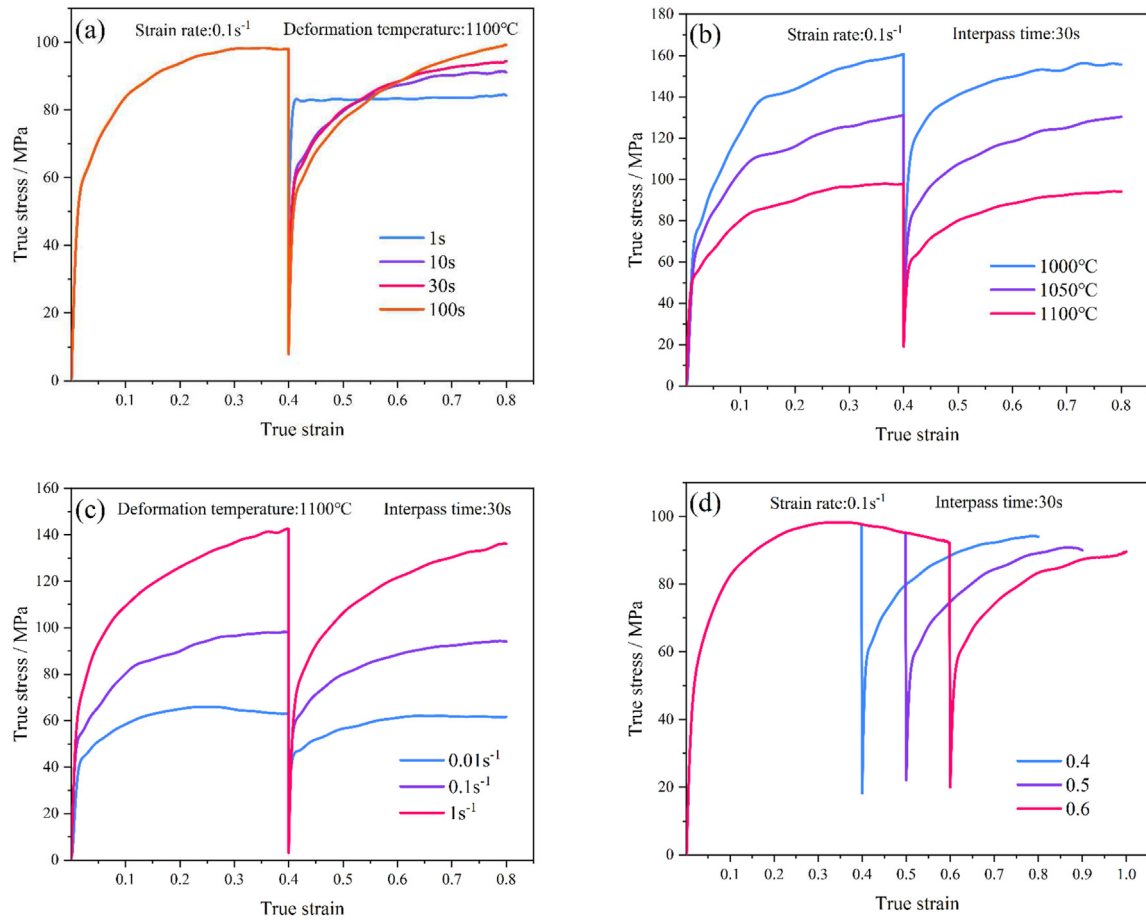
Fig. 4 − The metadynamic recrystallization flow stress curves of double-pass thermal compression tests. (a) Inter-pass times, (b) deformation temperatures, (c) strain rates, (d) pre-strains.

At 950 °C deformation temperature, the difference in yield stress between the first and second passes is larger than that at 1000 °C and 1050 °C, which indicates that SRX is weaker at lower deformation temperature. Fig. 3(c) shows the flow stress curves under different strain rates. Similar to the effect of deformation temperature, the flow stress gradually increases with increasing strain rate. Therefore, the higher the dislocation density of the material after the first thermal deformation, the higher the SRX driving force, which increases the SRX softening effect of the gap between passes. Fig. 3(d) shows the flow stress curves under different pre-strains. It can be seen from the figure that when pre-strain is 0.1 and 0.15, the deformation is small, and the softening effect is limited. When pre-strain increases to 0.2, the softening effect of the pass gap on the material is enhanced, which is due to the fact that increasing the pre-strain promotes the internal dislocation density of the grain and the deformation energy storage, which can provide a larger driving force for SRX and promote the SRX process.

3.1.2. Flow stress curve of MDRX

The flow stress curve of experimental steel in the state of inter-pass time, deformation temperature, strain rate and pre-strain is shown in Fig. 4. Fig. 4(a) shows the flow stress curves under different inter-pass times. It can be seen that the

second-pass flow stress has a significantly different trend with the inter-pass time, and the second-pass yield stress gradually decreases with the extension of inter-pass time, which is due to the MDRX softening effect becoming more and
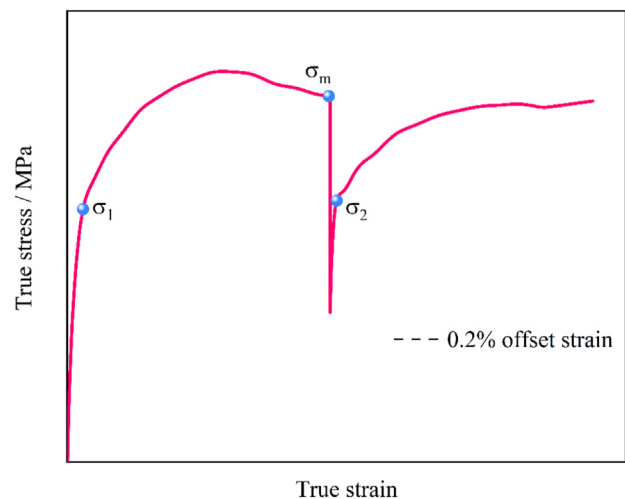

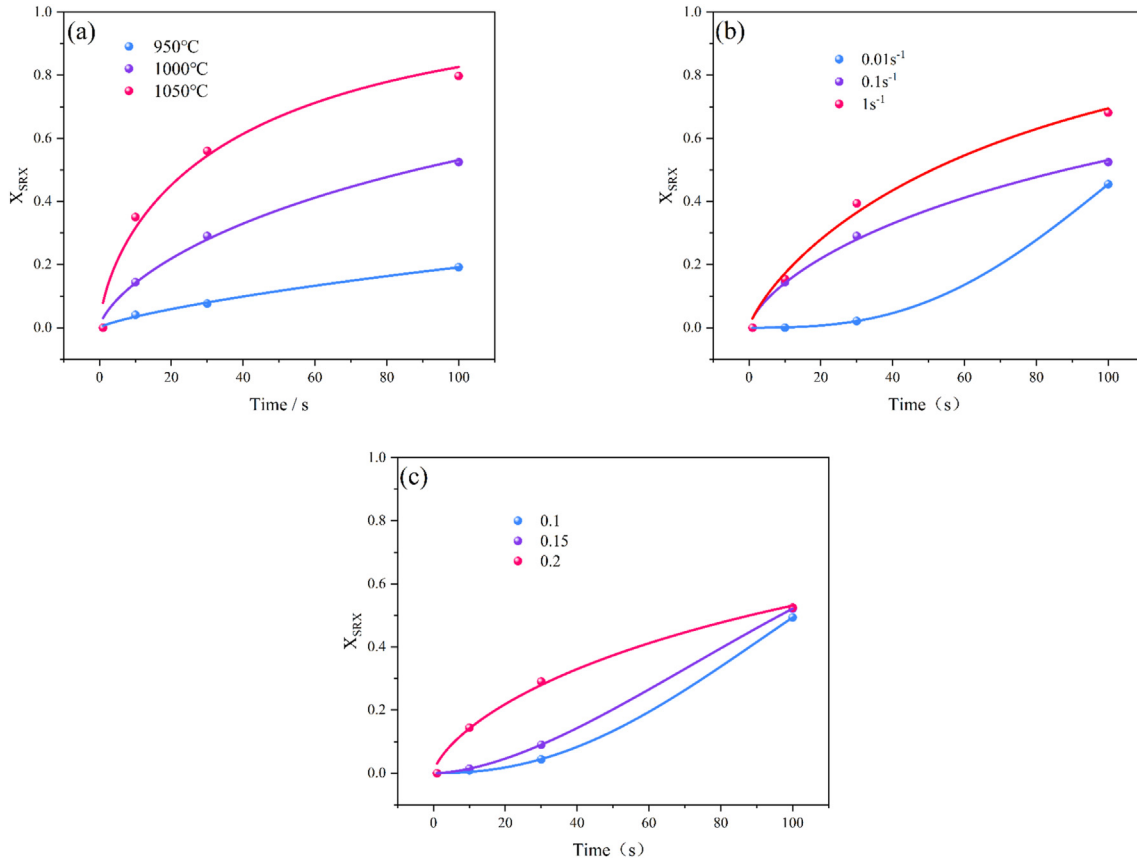**Fig. 5 − Schematic representations of 0.2% offset strain method.**

Fig. 6 − The SRX volume fraction under different deformation condition. (a) Deformation temperatures, (b) strain rates, (c) pre-strains.

more obvious with the increase of inter-pass time. The second-pass peak stress is slightly lower than the first peak stress, because the material undergoes DRX behavior in the first-pass, DRX nucleation is always present during deformation, and part of the grain boundaries migrate, and these nuclei do not need to be nurtured in the pass gap and grow, reducing the dislocation density of the material, thereby reducing the peak stress of the second-pass. Fig. 4(b) shows the flow stress curves under different deformation temperatures. It can be seen that the second flow stress changes with the change of deformation temperature, and the second-pass flow stress is slightly lower than the first-pass flow stress at 1000 °C, which indicates that the MDRX softening effect is limited under the current deformation temperature, and when the deformation temperature increases to 1100 °C, the second-pass flow stress is significantly reduced, which is due to the enhancement of MDRX softening effect and the increase of softening rate of the material. Fig. 4(c) shows the flow stress curves under different strain rates. With the decrease of strain rate, the softening rate decreases, and the second-pass flow stress almost coincides with the first-pass flow stress at a lower strain rate, which indicates that the MDRX softening rate is low in inter-pass. Deformation time shortens with the increase of the strain rate, and the dislocation density after deformation is increased, thereby increasing the MDRX driving force, and the softening effect becomes more obvious.

Fig. 4(d) shows the flow stress curves under different pre-strains. It can be seen that with the increase of pre-strain, the softening effect on the material is roughly the same, which is because when the first-pass strain exceeds the peak stress, DRX begins to nucleate, and increasing the pre-strain will not produce a large change in the DRX driving force, while MDRX does not need to be conceived and nucleated process, which is the DRX nucleus growth behavior, so it has less impact on MDRX.

3.1.3. The kinetics of SRX and MDRX

At present, five methods are available for calculating the static recrystallization softening rate of materials according to the flow stress data obtained from the double-pass thermal compression experiments, namely the compensation method (stress values corresponding to 0.2% or 2% strain), the post-interpolation method, the peak stress method [28], the average stress method, the maximum stress method, and the 5% total strain method. In this paper, the static softening rate is calculated using the 0.2% compensation method, and the schematic diagram of the 0.2% compensation method is shown in Fig. 5. F_{SRX} and F_{MDRX} are calculated as shown in Eq (1) [29,30]:

$$\begin{cases} F_{SRX} = \dfrac{\sigma_m - \sigma_2}{\sigma_m - \sigma_1} \\ F_{MDRX} = \dfrac{\sigma_m - \sigma_2}{\sigma_m - \sigma_1} \end{cases} \tag{1}$$

where σ_m is the flow stress at the first unloading, σ_2 is the stress value corresponding to 0.2% compensation method at the second deformation , σ_1 is the stress value corresponding to 0.2% compensation method at the first deformation.

According to Eq (1), the softening rate of SRX and MDRX can be calculated for the experimental steel under the action of various thermal deformation parameters at different inter-pass times. Considering the effect of recovery on material softening, according to Militzer and Sun theory [31,32], recrystallization is assumed to occur at a critical softening rate of 20%, so the volume fractions of SRX and MDRX can be calculated from Eq (2) [33]:

$$\begin{cases} X_{SRX} = \dfrac{F_{SRX} - 0.2}{1 - 0.2} \\ X_{MDRX} = \dfrac{F_{MDRX} - 0.2}{1 - 0.2} \end{cases} \tag{2}$$

where X_{SRX} is static recrystallization volume fraction, X_{MDRX} is metadynamic recrystallization volume fraction. According to Eq (2), X_{SRX} of experimental steel under different deformation conditions is calculated, as shown in Fig. 6. It can be seen that X_{SRX} increases as the inter-pass time increases, but at shorter inter-pass time, X_{SRX} is smaller, indicating that the SRX process needs time to nucleation. When strain rate is 0.1 s^{-1} and pre-strain is 0.2, X_{SRX} at deformation temperatures of 950 °C, 1000 °C, and 1050 °C is shown in Fig. 5(a). It can be seen from

the figure that the volume fraction of SRX decreases with the decrease of the deformation temperature. When the deformation temperature is 950 °C, X_{SRX} is below 20% for all inter-pass times, which indicates that at the lower deformation temperature, the dislocation is weaker, and thus the SRX process is inhibited, resulting in the dislocation generated in the pre-strain deformation not being completely eliminated [27,34]. When deformation temperature is 1000 °C and pre-strain is 0.2, X_{SRX} at strain rate state of 0.01 s^{-1}, 0.1 s^{-1} and 1 s^{-1} is shown in Fig. 6(b), With the increase of strain rate, the volume fraction of SRX increases continuously, which is due to the increase of dislocation density with the increase of strain rate, the time required to deform to the same strain decreases, thus increasing the deformation energy storage of the material. Meanwhile, with the increase of strain rate, the deformation time is shortened and the recovery is suppressed, which increases the dislocation density of the deformed material and provides a greater driving force for the SRX process and promotes the SRX process. When deformation temperature is 1000 °C and strain rate is 0.1 s^{-1}, X_{SRX} at pre-strain state of 0.1, 0.15 and 0.2 is shown in Fig. 6(c), it can be seen from the figure that when inter-pass time is 100 s, X_{SRX} is 49.39%, 52.18%, and 52.52%, respectively. With the increase of pre-strain, the volume fraction of SRX increases continuously. When pre-strain is 0.2, the softening effect on the material is most obvious and the volume fraction of SRX increases faster.
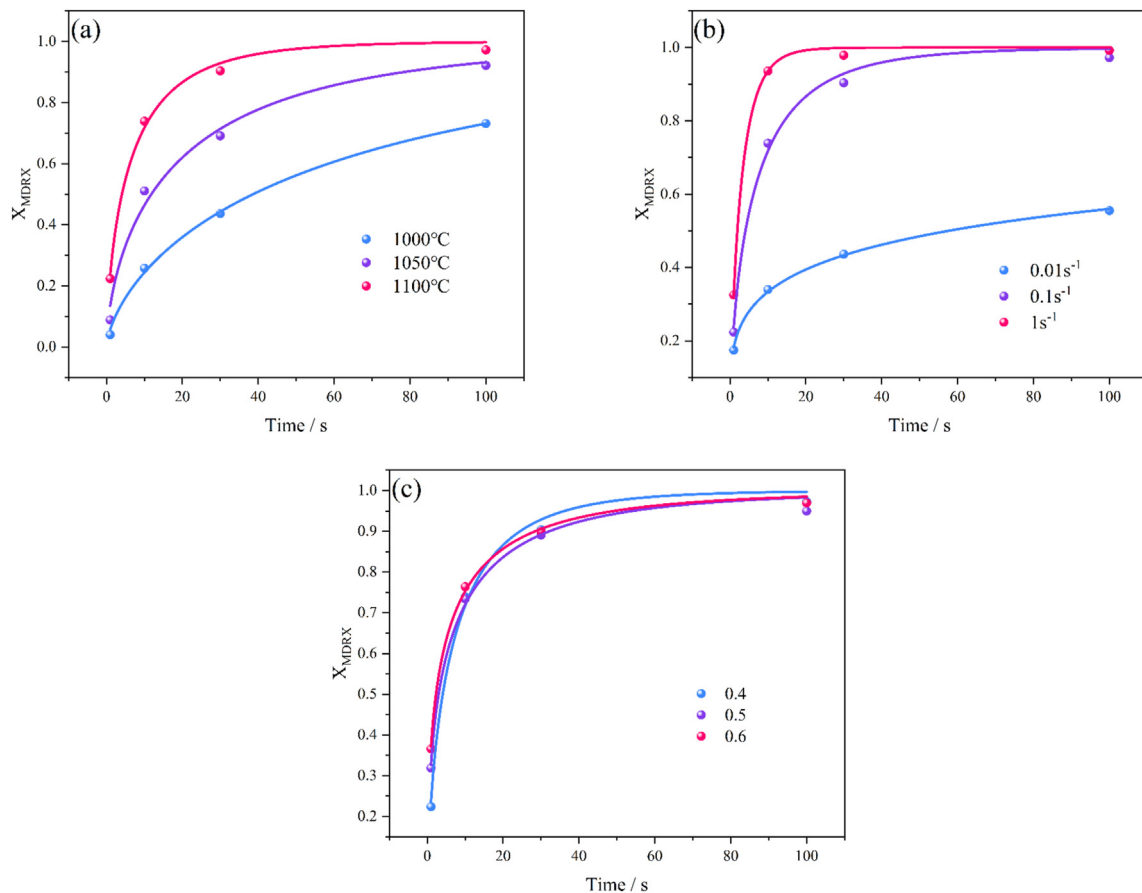

Fig. 7 — The MDRX volume fraction under different deformation condition. (a) Deformation temperatures, (b) strain rates, (c) pre-strains.
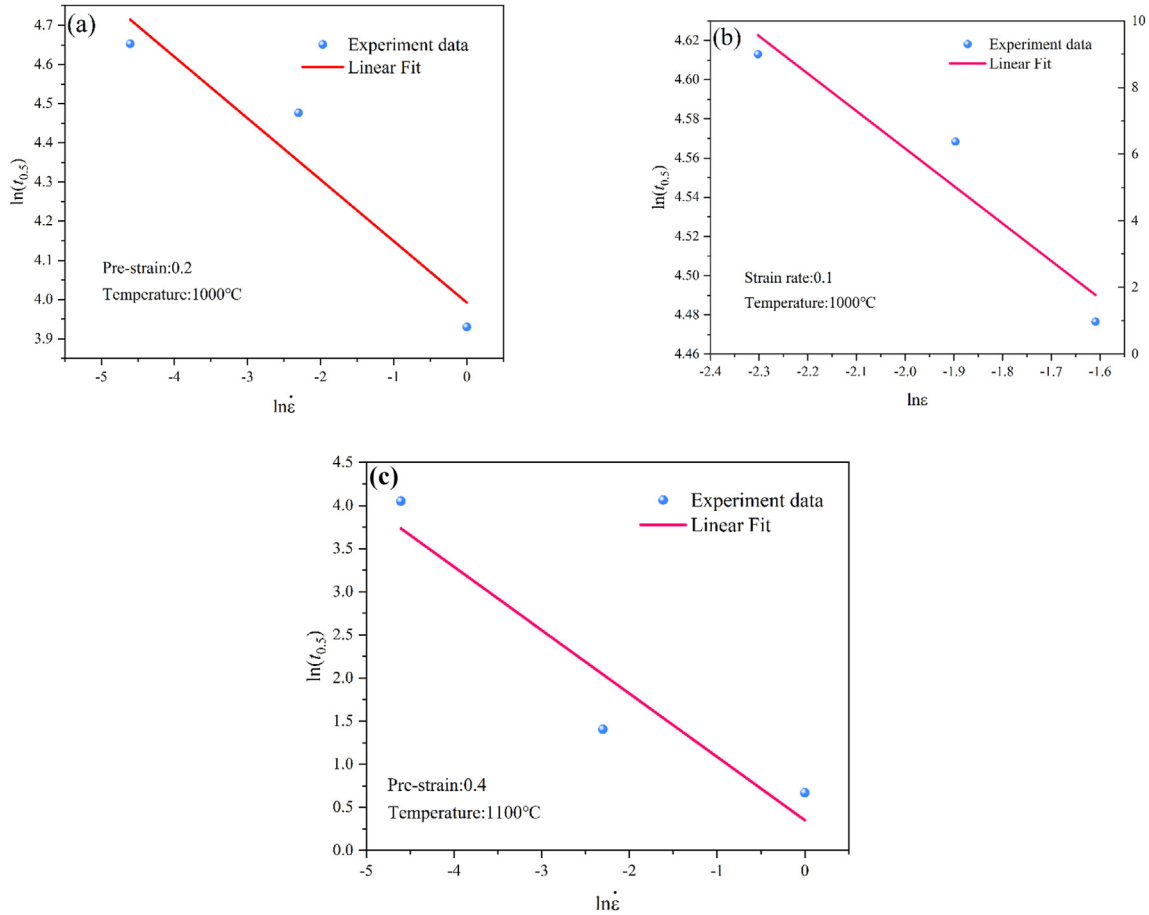
Fig. 8 − Relationship between (a) $lnt_{0.5SRX}$ versus $ln\dot{\varepsilon}$, (b) $lnt_{0.5SRX}$ versus $ln\dot{\varepsilon}$, (c) $lnt_{0.5MDRX}$ versus $ln\dot{\varepsilon}$.

This is because the grain deformation degree is larger under the higher pre-strain state, which is conducive to increasing the internal dislocation density of the grains and increasing the deformation energy storage, thus increasing the SRX driving force and promoting the SRX process [35].

According to Eq (2), X_{MDRX} of experimental steel under different deformation conditions is calculated, as shown in Fig. 7. It can be seen that X_{MDRX} increases as inter-pass time increases, when inter-pass time is larger and exceeds a certain value, the increase rate of X_{MDRX} gradually becomes slow.

When strain rate is 0.1 s^{-1} and pre-strain is 0.4, X_{MDRX} at deformation temperatures of 1000 °C, 1050 °C, and 1100 °C are shown in Fig. 7(a). It can be seen that the volume fraction of MDRX increases with the increase of the deformation temperature. The time required for X_{MDRX} to reach 50% at 1000 °C, 1050 °C and 1100 °C is 38.61 s, 11.82 s and 4.08 s,

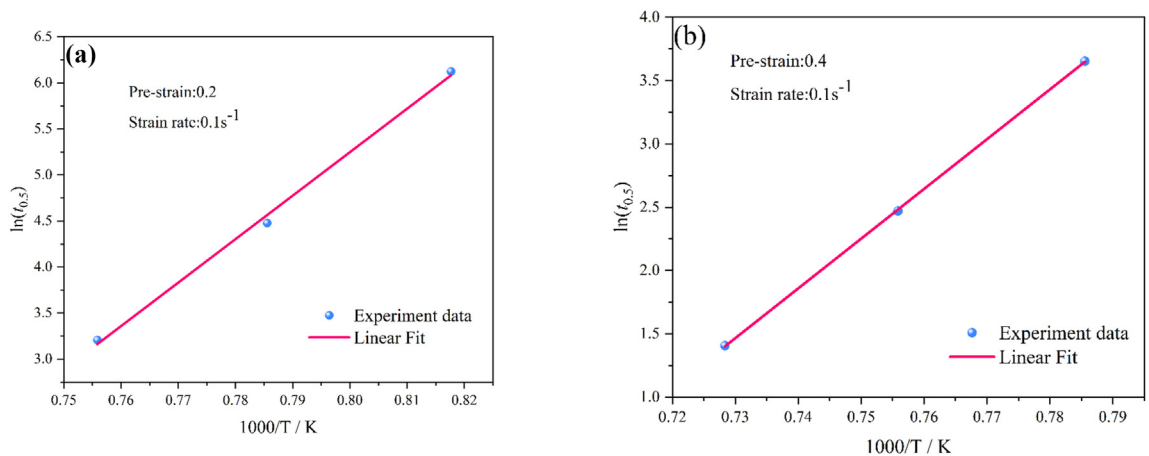
Fig. 9 − Relationship between (a) $lnt_{0.5SRX}$ versus $1/T$, (b) $lnt_{0.5MDRX}$ versus $1/T$.

respectively, due to the fact that MDRX is a thermally activated process [36-38]. The main feature is the DRX grain growth process, which is driven by grain boundary migration to reduce the grain boundary energy process during inter-pass time. In the higher deformation temperature state, the dislocation motility is enhanced, which facilitates the dislocation diffusion and increases the grain boundary migration rate, thus accelerating the MDRX process and promoting the rapid increase of X_{MDRX}. When deformation temperature is 1100 °C and pre-strain is 0.4, X_{MDRX} at different strain rates of $0.01\,s^{-1}$, $0.1\,s^{-1}$ and $1\,s^{-1}$ are shown in Fig. 7(b). With the increase of strain rate, X_{MDRX} continues to increase, and the time required for the X_{MDRX} to reach 50% is 57.49 s, 4.08 s and 1.95 s, respectively. This is due to the shortening of the time required to reach the same amount of deformation as the strain rate increases, and MDRX as a continuation process of DRX at the end of thermal deformation, the DRX nucleation is formed when the critical dislocation density in the grain bow-bending projection region during deformation exceeds a critical value, and the non-uniform dislocation gradient is more likely to form in the grain boundary region at higher strain rate states, increasing the DRX-shaped nucleation region, thus facilitating the MDRX process [39]. In addition, with the increase of strain rate, the recovery effect gradually decreases, which improves the deformation energy storage and dislocation density of the material during the deformation process, thus

increasing the MDRX driving force and promoting the MDRX process [8]. When deformation temperature is 1100 °C and strain rate is 0.1 s^{-1}, X_{MDRX} at different pre-strains of 0.4, 0.5 and 0.6 are shown in Fig. 7(c). The time required to reach 50% of X_{MDRX} with the increase of pre-strain is 4.08 s, 3 s and 2.31 s, respectively. It can be seen from the figure that X_{MDRX} is not very significant as the pre-strain increase. And the corresponding X_{MDRX} is basically consistent in the same pass gap time. This is because when the deformation of the first-pass exceeds the peak strain, increasing the pre-strain has little effect on the microscopic substructure of the material, and thus has little effect on MDRX.

The kinetic models of SRX and MDRX are generally expressed in the form of Avrami equations [40,41]. Since MDRX is less affected by pre-strain and initial grain size [10], the MDRX kinetic model in this paper ignores the influence of these two factors, and apply Eq (3) to calculate X_{SRX} and X_{MDRX}:

$$\begin{cases} X_{SRX} = 1 - \exp\left[-0.693\left(\dfrac{t}{t_{0.5SRX}}\right)^n\right] \\ X_{MDRX} = 1 - \exp\left[-0.693\left(\dfrac{t}{t_{0.5MDRX}}\right)^n\right] \end{cases} \quad (3)$$

where $t_{0.5SRX}$ and $t_{0.5MDRX}$ are the time for the recrystallizing volumetric fraction of 50%, t is the inter-pass time, and n is the material correlation coefficient. $t_{0.5SRX}$ and $t_{0.5MDRX}$ can be expressed by Eq (4) [42,43]:
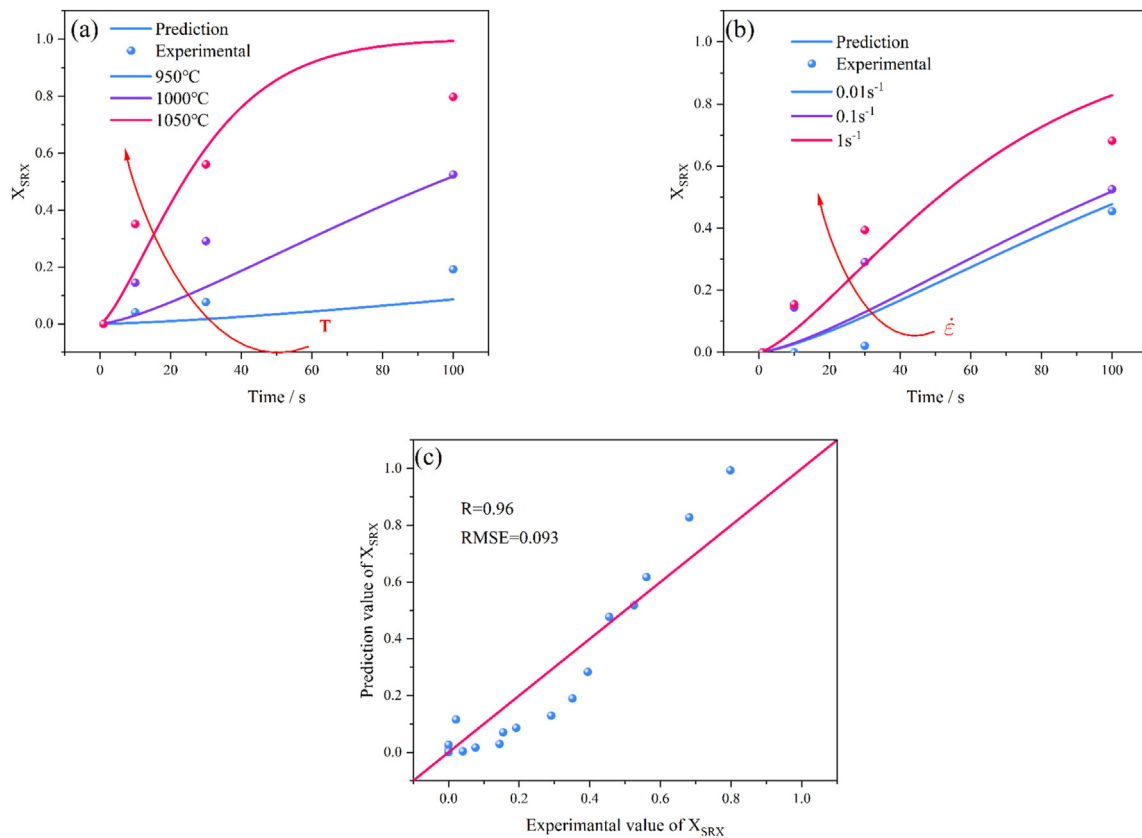

Fig. 10 — Comparison between predicted and experimental volume fraction of SRX. (a) Deformation temperatures, (b) strain rates, (c) comparison of predicted and experimental values at all deformation conditions.

$$\begin{cases} t_{0.5SRX} = A_{SRX}\dot{\varepsilon}^p \varepsilon^q \exp\left(\frac{Q_{SRX}}{RT}\right) \\ t_{0.5MDRX} = A_{MDRX}\dot{\varepsilon}^r \exp\left(\frac{Q_{MDRX}}{RT}\right) \end{cases} \quad (4)$$

where A_{SRX}, A_{MDRX}, p, and q are material dependent constants , Q_{SRX} is the static recrystallization activation energy, and Q_{MDRX} is the metadynamic recrystallization activation energy. It can be seen from Eq (4) that $t_{0.5SRX}$ is a function related to deformation temperature, strain rate, and pre-strain, and $t_{0.5MDRX}$ is a function related to deformation temperature and strain rate, which is also consistent with the conclusion of the analysis in the previous section. When A_{MDRX}, Q_{MDRX}, n, r, p, q, A_{SRX} and Q_{SRX} values in Eq (3) and Eq (4) are calculated, the SRX and MDRX kinetic model can be established. Taking the logarithm on both sides of Eq (3) to obtain Eq (5):

$$\begin{cases} ln\left[ln\left(\frac{1}{1-X_{SRX}}\right)\right] = ln\,0.693 + nln\left(\frac{t}{t_{0.5SRX}}\right) \\ ln\left[ln\left(\frac{1}{1-X_{MDRX}}\right)\right] = ln\,0.693 + nln\left(\frac{t}{t_{0.5MDRX}}\right) \end{cases} \quad (5)$$

The X_{SRX} and X_{MDRX} are corresponding to various inter-pass times under different deformation temperatures, strain rates, and pre-strains is brought into Eq (5), and $t_{0.5SRX}$, $t_{0.5MDRX}$ and n for different heat deformation states can be obtained by

non-linear fitting. The n values of SRX and MDRX are 1.38 and 0.625. It is important to note here that the value of n changes with the type of material and experimental conditions [44].

To further calculate Q_{SRX} and Q_{MDRX}, take the logarithm of both sides of Eq (4) to obtain Eq (6):

$$\begin{cases} lnt_{0.5SRX} = lnA_{SRX} + pln\dot{\varepsilon} + qln\varepsilon + \frac{Q_{SRX}}{RT} \\ lnt_{0.5MDRX} = lnA_{MDRX} + rln\dot{\varepsilon} + \frac{Q_{MDRX}}{RT} \end{cases} \quad (6)$$

By calculating the values corresponding to X_{SRX}, X_{MDRX} for different inter-pass times, $t_{0.5SRX}$, $t_{0.5MDRX}$ corresponding to the time when X_{SRX}, X_{MDRX} reaches 50% can be obtained. When the deformation temperature, pre-strain, and strain rate are constant, the values of p, q and r can be expressed as Eq (7):

$$\begin{cases} p = \left.\frac{\partial lnt_{0.5SRX}}{\partial ln\dot{\varepsilon}}\right|_{T,\varepsilon} \\ q = \left.\frac{\partial lnt_{0.5SRX}}{\partial ln\,\varepsilon}\right|_{T,\dot{\varepsilon}} \\ r = \left.\frac{\partial lnt_{0.5MDRX}}{\partial ln\dot{\varepsilon}}\right|_{T} \end{cases} \quad (7)$$

The relationship between $ln\,t_{0.5SRX}$ and $ln\dot{\varepsilon}$, $lnt_{0.5SRX}$ and $ln\,\varepsilon$, $ln\,t_{0.5MDRX}$ and $ln\dot{\varepsilon}$ are shown in Fig. 8. The p value is −0.157, the q value is −0.191 and the r value is −0.734 through linear
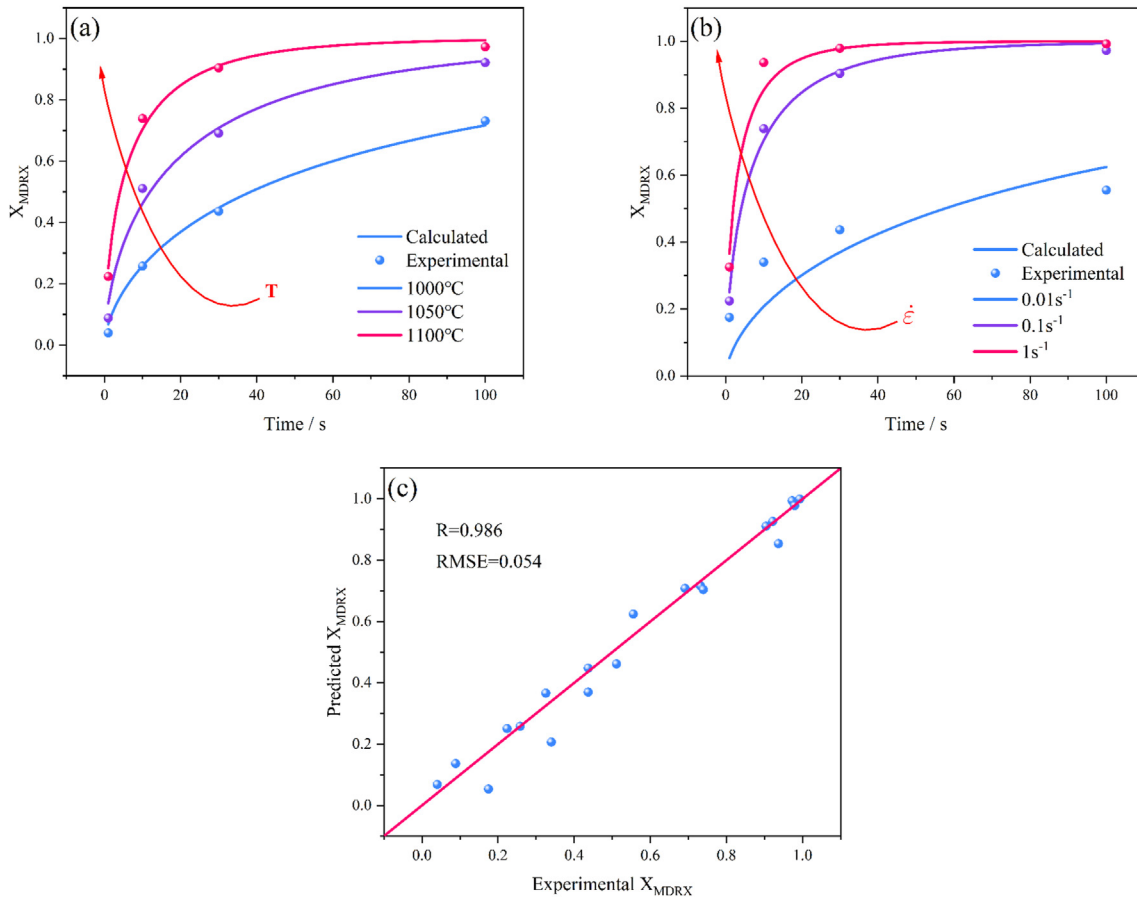

Fig. 11 — Comparison between predicted and experimental volume fraction of MDRX. (a) Deformation temperatures, (b) strain rates, (c) comparison of predicted and experimental values at all deformation conditions.
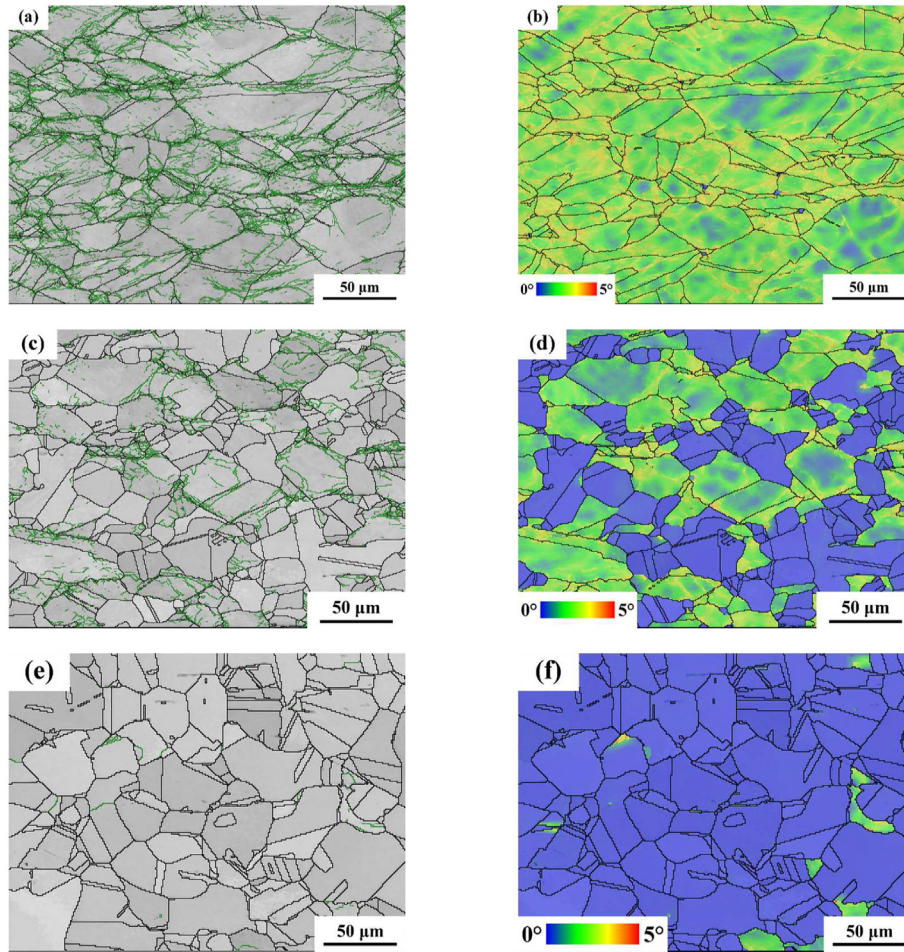
Fig. 12 − Grain boundary and local misorientation map of the experimental steel deformed at strain rate 0.1 s⁻¹, inter-pass time 30 s and pre-strain 0.2 with deformation temperatures of 950 °C, 1000 °C and 1050 °C. (a) GB map at temperature of 950 °C, (b) LocMis map of (a), (c) GB map at temperature of 1000 °C, (d) LocMis map of (c), (e) GB map at temperature of 1050 °C, (f) LocMis map of (e).

fitting. The r value obtained in this paper is consistent with the value of most existing studies in the range of -0.8 to -0.33. When the strain rate and pre-strain are constants, Q_{SRX} and Q_{MDRX} can be calculated by Eq (8):

$$\begin{cases} Q_{SRX} = R \dfrac{\partial \ln t_{0.5SRX}}{\partial(1/T)}\bigg|_{\varepsilon,\dot{\varepsilon}} \\[3mm] Q_{MDRX} = R \dfrac{\partial \ln t_{0.5MDRX}}{\partial(1/T)}\bigg|_{\dot{\varepsilon}} \end{cases} \quad (8)$$

The relationship between $\ln t_{0.5SRX}$ and $1/T$, $\ln t_{0.5MDRX}$ and $1/T$ are shown in Fig. 9. The Q_{SRX} value is 392.59 kJ/mol and the Q_{MDRX} value is 326.61 kJ/mol obtained by linear fitting and mathematical operation, and the A_{SRX} value is 3.83×10^{-15} and the A_{MDRX} value is 2.8×10^{-13} calculated by bringing all the deformation parameters and correlation coefficients into Eq (6).

Based on the above assumptions, the kinetic models of SRX and MDRX of the experimental steel are shown in Eqs (9) and (10):

$$\begin{cases} X_{SRX} = 1 - \exp\left[-0.693 \left(\dfrac{t}{t_{0.5SRX}} \right)^{1.47} \right] \\[4mm] X_{MDRX} = 1 - \exp\left[-0.693 \left(\dfrac{t}{t_{0.5MDRX}} \right)^{0.625} \right] \end{cases} \quad (9)$$

$$\begin{cases} t_{0.5SRX} = 3.83 \times 10^{-15} \dot{\varepsilon}^{-0.157} \varepsilon^{-0.191} \exp\left(\dfrac{392590}{RT} \right) \\[4mm] t_{0.5MDRX} = 2.8 \times 10^{-13} \dot{\varepsilon}^{-0.734} \exp\left(\dfrac{326611}{RT} \right) \end{cases} \quad (10)$$

To verify the accuracy of the established model, the predicted and experimental values of X_{SRX} and X_{MDRX} under different thermal deformation process states are compared, and the results are shown in Figs. 10 and 11. It can be seen that the experimental values are in good agreement with the predicted values, indicating that the kinetic models of SRX and MDRX can be used to predict the softening behavior of the experimental steel.

3.2. Effect of deformation state on static softening behavior

3.2.1. Deformation temperature

Fig. 12(a)—(f) shows the EBSD characterization of the experimental steel at pre-strain of 0.2, strain rates of 0.1 s^{-1}, inter-pass time of 30 s, and deformation temperature of 950 °C, 1000 °C and 1050 °C, respectively. It can be seen from the figure that with the increase in deformation temperature, the grains gradually become flat and grow up. This is due to the fact that SRX is a thermally activated process, and the dislocation movement is more intense at higher deformation temperatures which accelerates grain boundary migration and grain growth. It also can be seen from the figure that the microscopic substructure inside the grains at the deformation temperature of 950 °C is greater than that at 1000 °C and 1050 °C, which also indicates that the dislocation movement ability of the material is lower at the lower deformation temperature state, and the SRX process is not easily induced.

When deformation temperature is 1050 °C, the local orientation difference within the material is lower and more uniformly distributed, indicating that the dislocation density within the grains is lower under the current deformation conditions and a complete SRX process occurs. This also echoes the flow stress analysis of SRX under different deformation temperature states in the previous section, and the SRX process can be promoted at higher deformation temperatures.

Fig. 13(a)—(f) shows the EBSD characterization of the experimental steel at pre-strain of 0.4, strain rates of 0.1 s^{-1}, inter-pass time of 30 s, and deformation temperature of 1000 °C, 1050 °C and 1100 °C, respectively. It can be seen from the figure that with the increase of deformation temperature, the grain size continues to increase, and fine recrystallization grains can be observed near the larger grains, these fine grains are DRX nucleation or initial DRX grains. When deformation temperature increases, the smaller grains gradually evolve into coarse equiaxed grains, the reason for this phenomenon
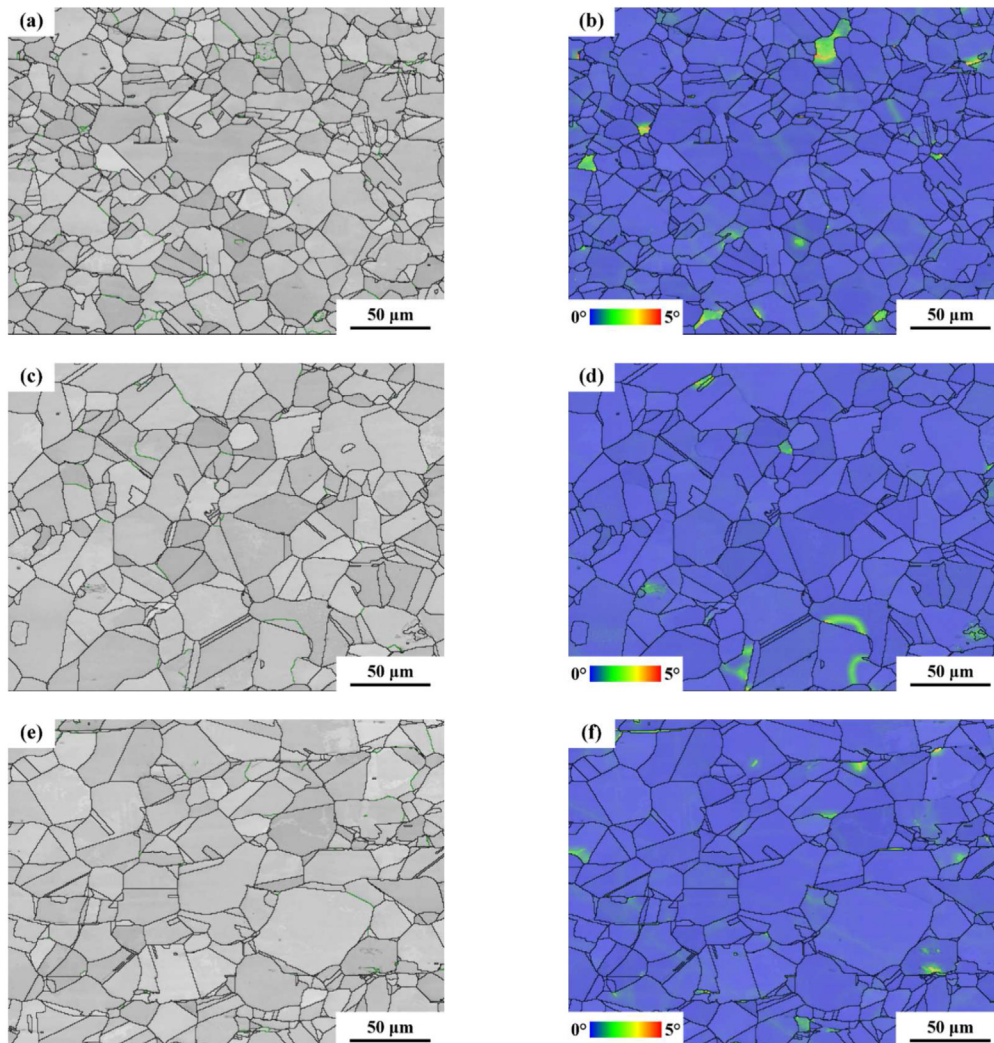

Fig. 13 — Grain boundary and local misorientation map of the experimental steel deformed at strain rate 0.1 s^{-1}, inter-pass time 30 s and pre-strain 0.4 with deformation temperatures of 1000 °C, 1050 °C and 1100 °C. (a) GB map at temperature of 1000 °C, (b) LocMis map of (a), (c) GB map at temperature of 1050 °C, (d) LocMis map of (c), (e) GB map at temperature of 1100 °C, (f) LocMis map of (e).

is that with the increase of deformation temperature, the atom and dislocation diffusion movement is strengthened, the high grain boundary migration rate promotes large angular grain boundaries migration, and the grain migrates rapidly in the form of strain-driven interface migration. In addition, the increase in deformation temperature also accelerates the recovery process, which is conducive to grain growth and promotes the MDRX process [45].

3.2.2. Strain rate

Fig. 14(a)–(f) shows the EBSD characterization of the experimental steel at deformation temperature of 1000 °C, pre-strain of 0.2, inter-pass time of 30 s, and strain rate of 0.01 s^{-1}, 0.1 s^{-1} and 1 s^{-1}, respectively. It can be seen from the figure that with the increase of strain rate, the grain size gradually decreases, which is due to the fact that the higher strain rate increases the dislocation motility, shortens the deformation time required to reach the same deformation, and suppresses the effect of recovery. The increased dislocation density after

deformation increases the deformation energy storage, providing a more significant driving force for SRX. When strain rate is 1 s^{-1}, there is less microscopic substructure within the grain, less local orientation difference and higher degree of SRX. The increase in strain rate has a grain refinement effect on the experimental steel.

Fig. 15(a)–(f) shows the EBSD characterization of the experimental steel at deformation temperature of 1100 °C, pre-strain of 0.4, inter-pass time of 30 s, and strain rate of 0.01 s^{-1}, 0.1 s^{-1} and 1 s^{-1}, respectively. It can be seen from the figure that the grain size at low strain rates is much larger than at high strain rates. This is because high strain rates increase the storage energy of the thermally deformed material, which increases the number of recrystallized nuclei in the austenite, thus allowing metadynamic recrystallisation to be completed more fully in the inter-pass time, and the smaller the metadynamic recrystallized grain size obtained. More equiaxial grains without distortion replace the deformed grains, therefore the grains are more homogeneous [9], which indicates
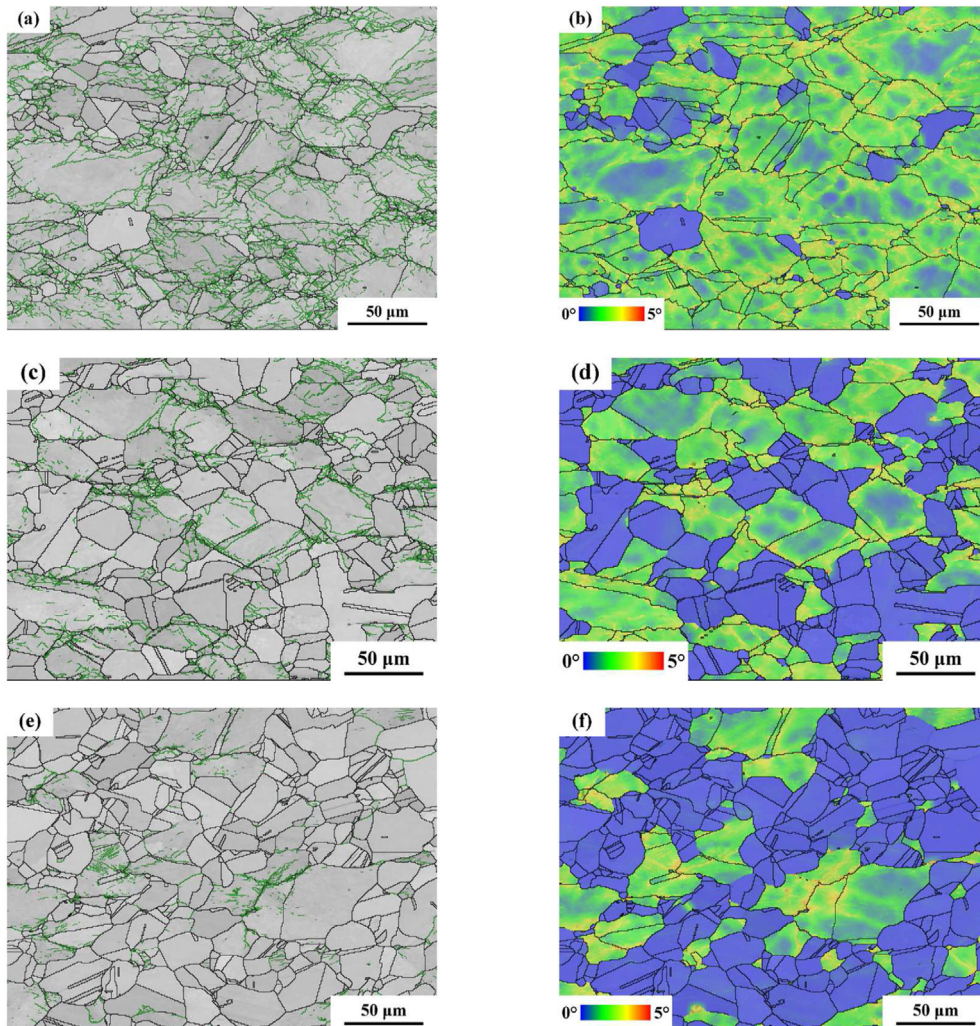

Fig. 14 – Grain boundary and local misorientation map of the experimental steel deformed at strain rates of 0.01 s^{-1}, 0.1 s^{-1}, and 1 s^{-1}, inter-pass time 30 s at deformation temperature 1000 °C and pre-strain 0.2. (a) GB map at strain rate of 0.01 s^{-1}, (b) LocMis map of (a), (c) GB map at strain rate of 0.1 s^{-1}, (d) LocMis map of (c), (e) GB map at strain rate of 1 s^{-1}, (f) LocMis map of (e).

that the degree of MDRX increases with the increase of strain rate. This is due to the fact that when the strain rate is higher, the dislocation motion is enhanced, the deformation time is shortened to reduce the migration time of large angular grain boundaries, and some grains generate DRX grains by the CDRX mechanism, which promotes the deformation matrix and recrystallization grain energy storage difference, which increases the migration rate of grain boundaries and promotes MDRX.

3.2.3. Strain

Fig. 16(a)—(f) shows the EBSD characterization of the experimental steel at deformation temperature of 1000 °C, strain rate of 0.1 s^{-1}, inter-pass time of 30 s, and pre-strain of 0.1, 0.15 and 0.2, respectively. It can be seen from the figure that the grain size changes less at pre-strain of 0.1 and 0.15, which indicates that pre-strain has little effect on SRX grain size. However, the SRX volume fraction is higher at pre-strain of 0.2

than at pre-strain of 0.1 and 0.15, suggesting that the SRX grain boundary migration has a greater effect on reducing the dislocation density than dislocation cross-slip and climbing during recovery [46,47]. The higher pre-strain increases the internal dislocation density of the material, which increases the deformation energy storage and provides a more significant driving force for the SRX, increasing the SRX volume fraction. However, as the SRX process involves grain gestation, nucleation, and growth, pre-strain has less influence on SRX than strain rate and deformation temperature at an inter-pass time of 30 s.

Fig. 17(a)—(f) shows the EBSD characterization of the experimental steel at deformation temperature of 1100 °C, strain rate of 0.1 s^{-1}, inter-pass time of 30 s, and pre-strain of 0.4, 0.5 and 0.6, respectively. It can be seen from the figure that the main factors affecting the grain boundary migration are deformation temperature and strain rate, and the change of pre-strain has less effect on the MDRX volume fraction. It can
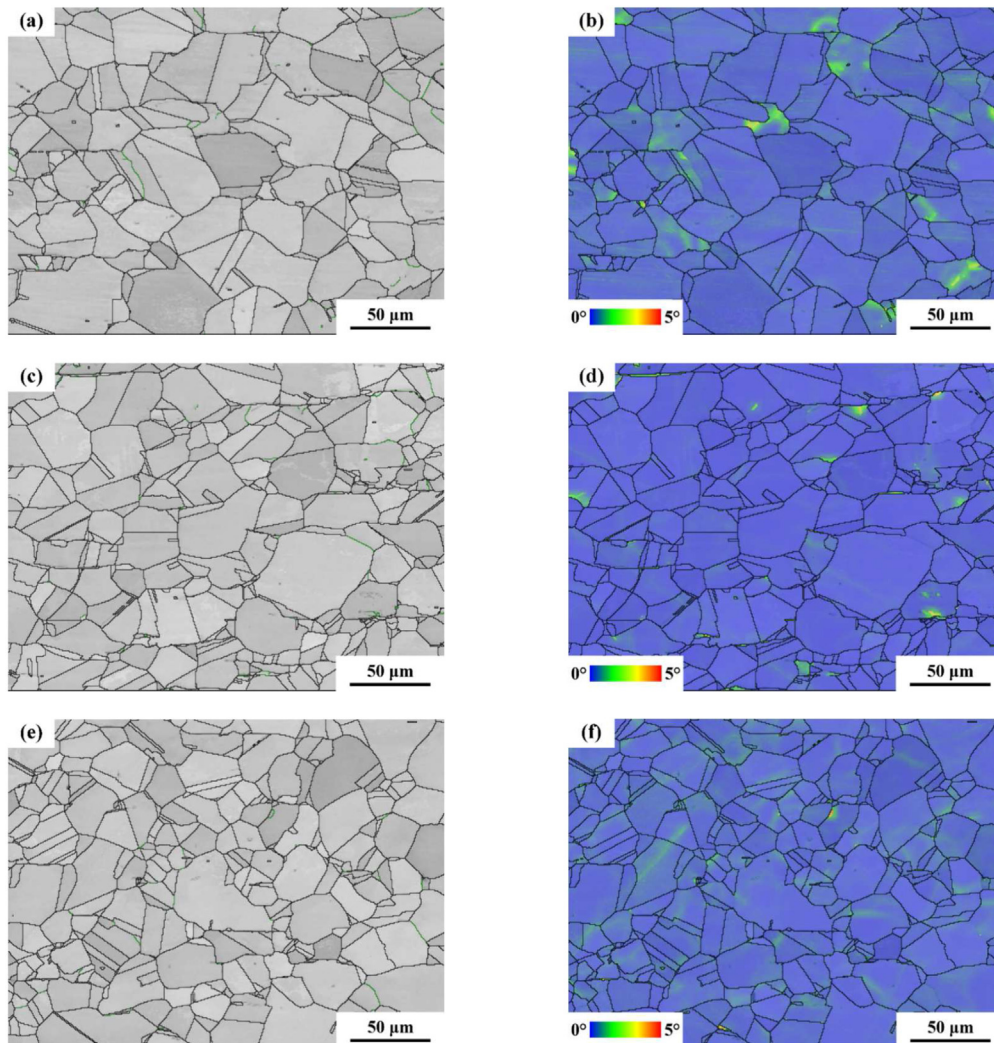

Fig. 15 — Grain boundary and local misorientation map of the experimental steel deformed at strain rates of 0.01 s^{-1}, 0.1 s^{-1}, and 1 s^{-1}, inter-pass time 30 s at deformation temperature 1100 °C and pre-strain 0.4. (a) GB map at strain rate of 0.01 s^{-1}, (b) LocMis map of (a), (c) GB map at strain rate of 0.1 s^{-1}, (d) LocMis map of (c), (e) GB map at strain rate of 1 s^{-1}, (f) LocMis map of (e).
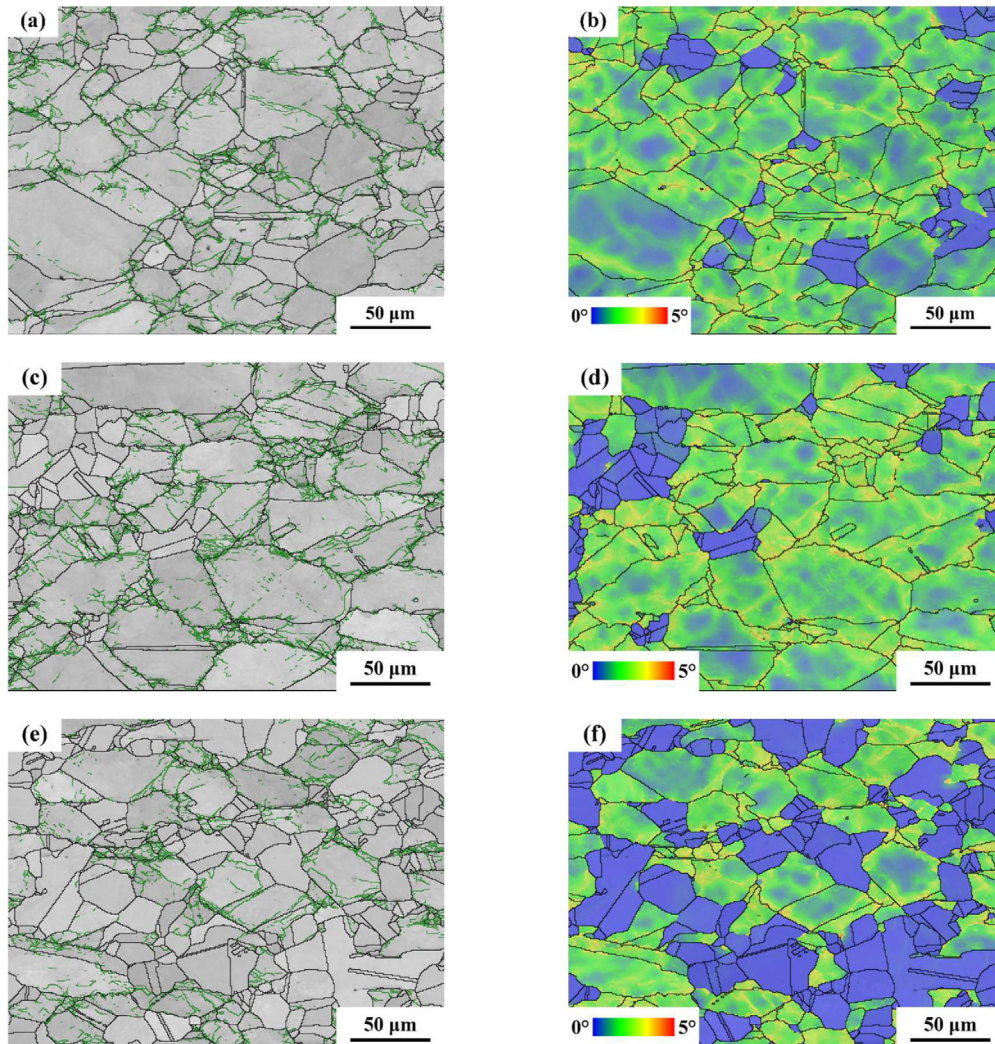
Fig. 16 – Grain boundary and local misorientation map of the experimental steel deformed at strain rate 0.1 s⁻¹ under deformation temperature 1000 °C for inter-pass time of 30 s with pre-strain of 0.1, 0.15 and 0.2. (a) GB map at strain of 0.1, (b) LocMis map of (a), (c) GB map at strain of 0.15, (d) LocMis map of (c), (e) GB map at strain of 0.2, (f) LocMis map of (e).

be seen from the figure that in pre-strain 0.4 and 0.5, the grain size change is small, MDRX microstructure is relatively similar. This is because under the experimental scheme in this paper, the pre-strain of the material exceeds the peak strain of the experimental steel, the increase in strain has less effect on the internal microscopic substructure of the material, less change in deformation energy storage difference, and less effect on MDRX, which also verifies that MDRX is mainly the grain growth process of the inter-pass, and the grain growth needs to be achieved by grain boundary migration, When pre-strain is 0.6, it is obvious that the grain size is larger than pre-strain 0.4 and 0.5, which is because the material is in the steady-state stress range at this time, the material enters the complete DRX stage, and the DRX grain completely replaces the deformed grains of the original structure during the deformation process, therefore only the growth process of DRX grain occurs in the pass gap, the degree of MDRX in inter-pass is higher, and the grain size is significantly larger.

3.2.4.   Inter-pass time

Fig. 18(a)–(h) shows the EBSD characterization of the experimental steel at deformation temperature of 1100 °C, strain rate of 0.1 s⁻¹, pre-strain of 0.2, and inter-pass time of 1 s, 10 s, 30 s, and 100 s, respectively. It can be seen from the figure that the original grains are polygonal after the pre-strain of deformation, and the grain boundaries are serrated, indicating that DRX behavior does not occur in this deformation condition, which is consistent with the occurrence of SRX characteristic behavior. As shown in Fig. 18(a) and (b), when inter-pass time is 1 s, it can be seen that the grain boundary migrates towards the center of curvature, which is due to the fact that when the grain boundary moves towards the center of curvature, it can promote the microstructure to reach a relatively stable energy state, thus reducing the grain boundary energy, and it can be seen that SRX grains has not completely produced in this deformation state, and the SRX volume fraction is small. From the local orientation
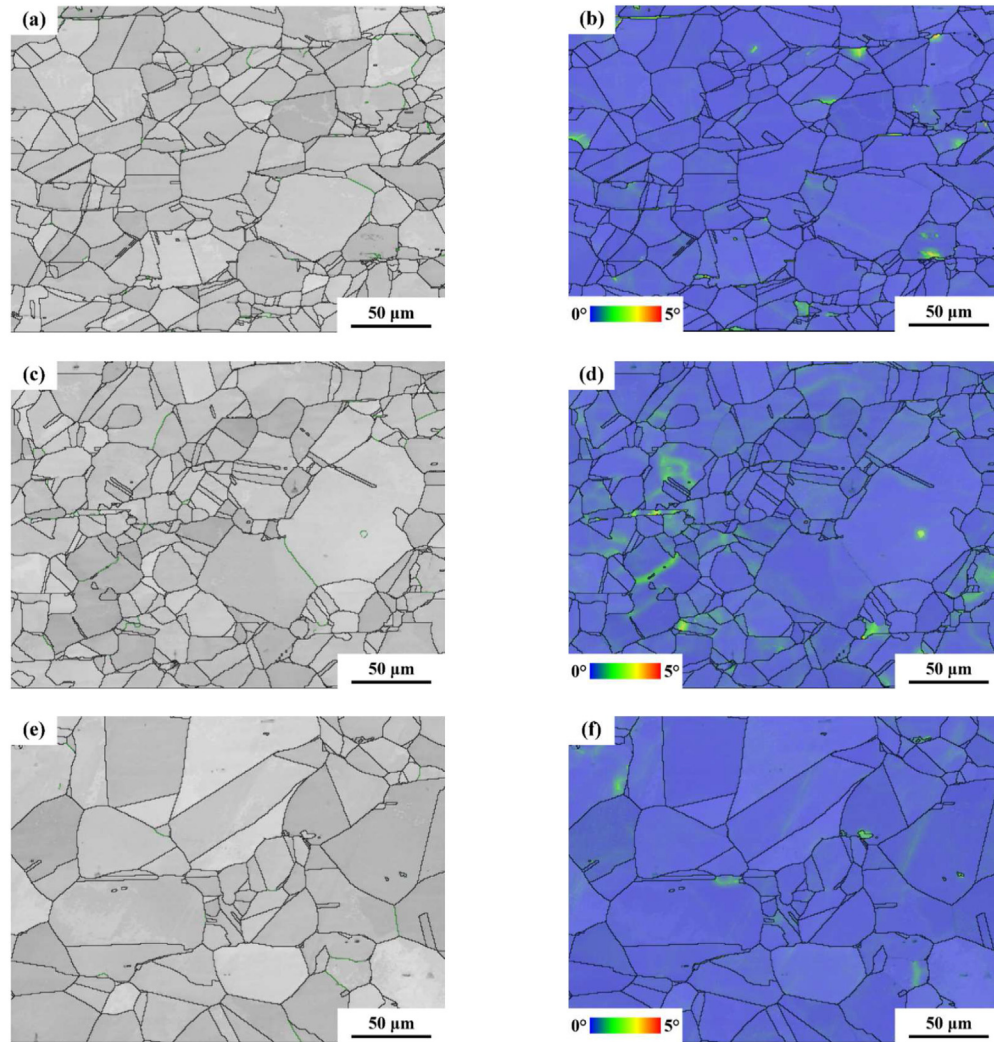
Fig. 17 — Grain boundary and local misorientation map of the experimental steel deformed at strain rate 0.1 s^{-1} under deformation temperature 1100 °C for inter-pass time of 30 s with pre-strain of 0.4, 0.5 and 0.6. (a) GB map at strain of 0.4, (b) LocMis map of (a), (c) GB map at strain of 0.5, (d) LocMis map of (c), (e) GB map at strain of 0.6, (f) LocMis map of (e).

difference, it can be found that the internal orientation difference of the grains is higher, reflecting the higher dislocation density. As shown in Fig. 18(c) and (d), when inter-pass time is 10 s, it can be seen that fine SRX grains are generated during the migration of large angular grain boundaries, the SRX volume fraction increases, and the local misorientation decreases with the increase of inter-pass time, which reduces the dislocation density. As shown in Fig. 18(e) and (f), when inter-pass time is 30 s, it can be seen that the internal microscopic substructure of the grains is further reduced. As shown in Fig. 18(g) and (h), when inter-pass time is 100 s, no new SRX grains are generated, indicating that the accumulated deformation storage energy is consumed completely in this state and the SRX behavior occurs completely, with a little change in SRX volume fraction. From this aspect, it can also be considered that the SRX process reduces internal defects and substructure so that the microstructure reaches a relatively stable state.

Fig. 19(a)—(h) shows the EBSD characterization of the experimental steel at deformation temperature of 1100 °C, strain rate of 0.1 s^{-1}, pre-strain of 0.4, and inter-pass times of 1 s, 10 s, 30 s, and 100 s, respectively. It can be seen from the figure that MDRX is much faster than SRX in different inter-pass times, and MDRX behavior occurs in the range of inter-pass time from 1 s to 100 s. As shown in Fig. 19(a) and (b), when inter-pass time is 1 s, the DRX nuclei grow rapidly in the inter-pass while reducing the internal microscopic substructure of the original deformed grains, and it can be seen from the local orientation map that most of the grains have small local orientation difference and the MDRX volume fraction increases [48]. As shown in Fig. 19(c)—(h), when inter-pass times are 10 s, 30 s and 100 s, it can be seen from the figure that the DRX grain produced by the first deformation basically completes the growth process, compared with the case of inter-pass time of 1 s, the MDRX grain growth process is more obvious, the local orientation difference changes are small,
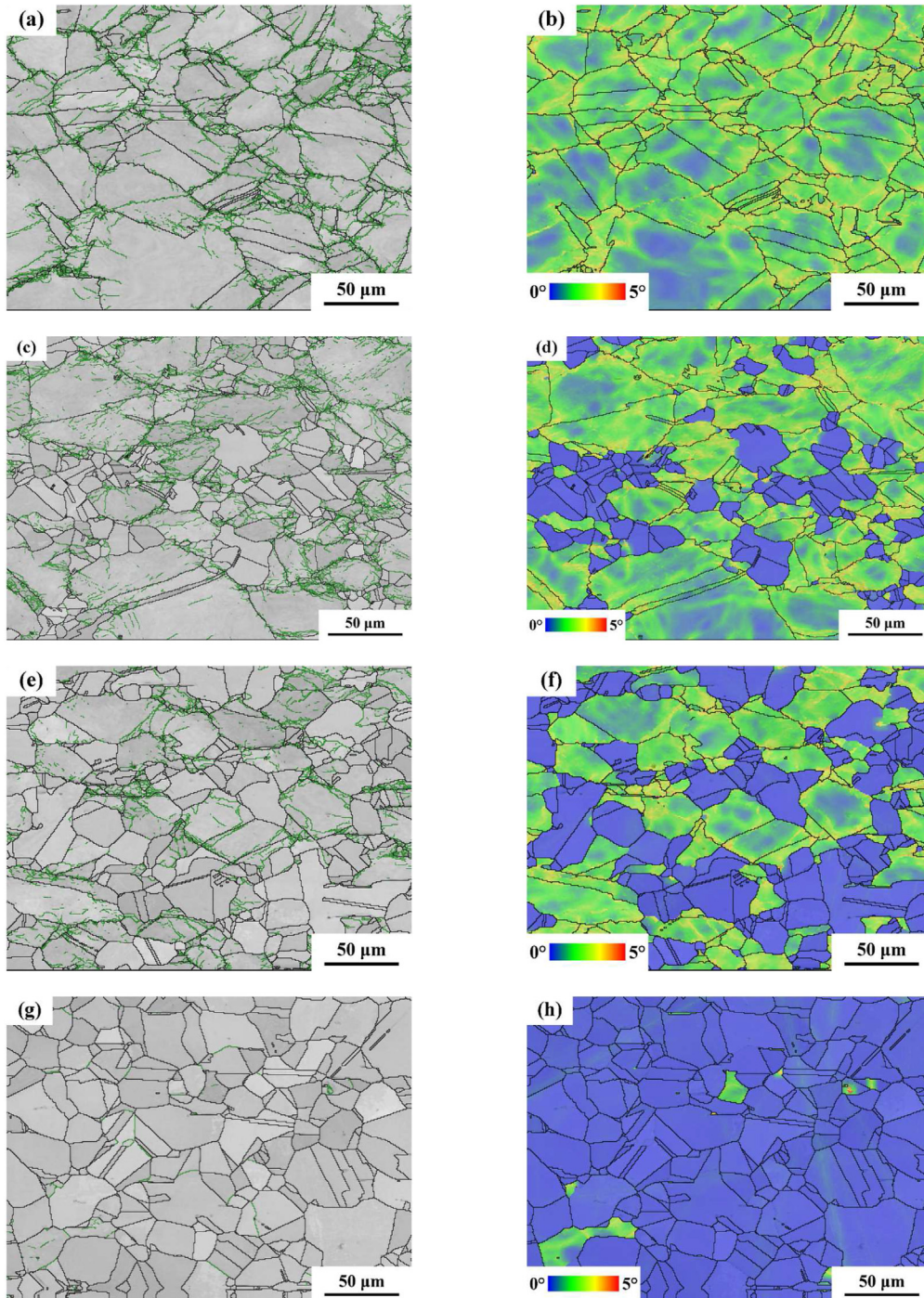
Fig. 18 — Grain boundary and local misorientation map of the experimental steel deformed at strain rate 0.1 s^{-1}, pre-strain 0.2, deformation temperatures of 1000 °C and inter-pass time of 1 s, 10 s, 30 s and 100 s. (a) GB map at inter-pass time of 1 s, (b) LocMis map of (a), (c) GB map at inter-pass time of 10 s, (d) LocMis map of (c), (e) GB map at inter-pass time of 30 s, (f) LocMis map of (e), (g) GB map at inter-pass time of 100 s, (h) LocMis map of (g).

and some smaller grains are swallowed by MDRX grains, the MDRX behavior is more adequate, and a complete MDRX process occurs, which indicates that the MDRX behavior in inter-pass time of 10 s range is basically completed. It can also be seen from the figure that the grain size increases as the MDRX volume fraction increases, and when the MDRX volume fraction is stable and MDRX is completed, the MDRX grain size remains basically unchanged.
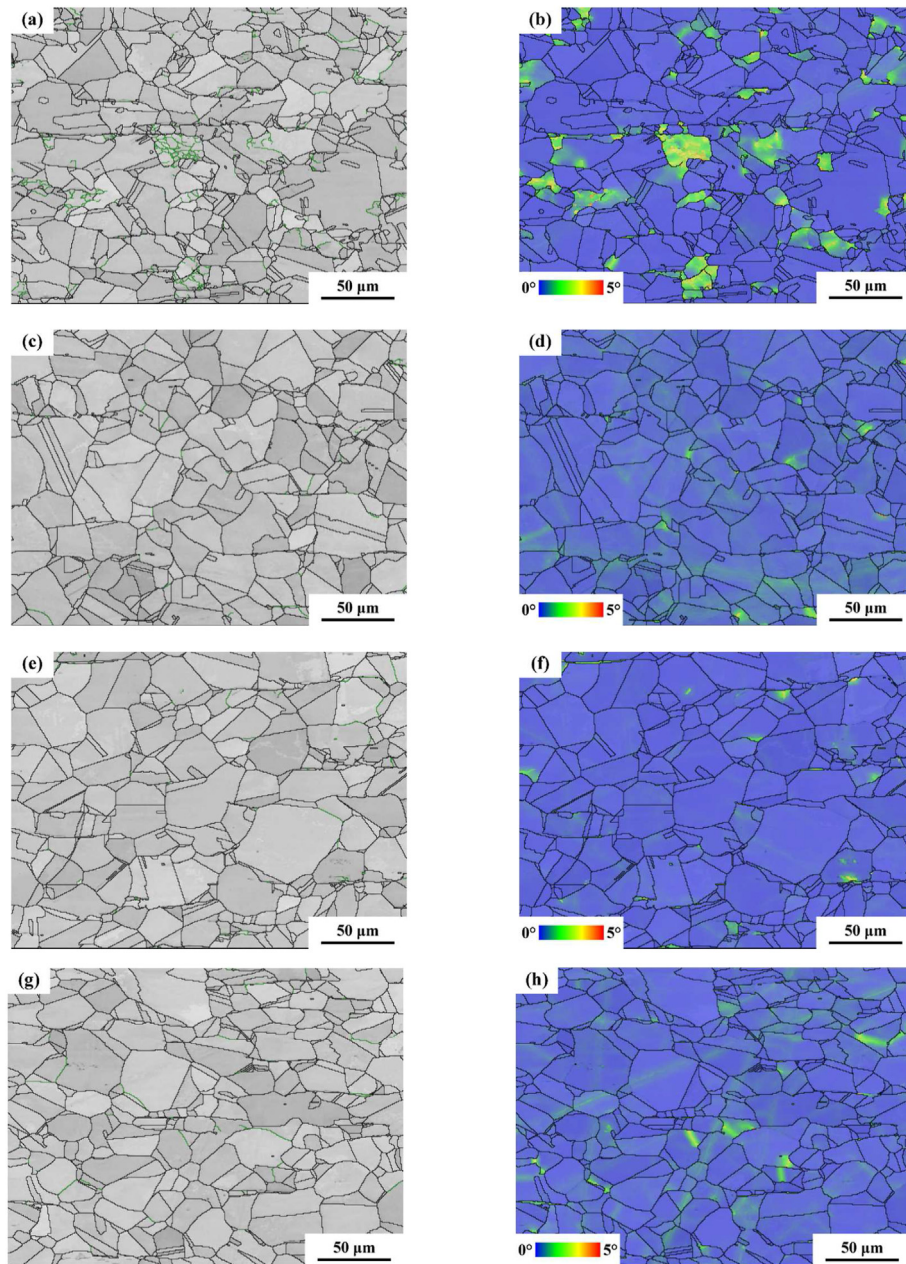
Fig. 19 — Grain boundary and local misorientation map of the experimental steel deformed at strain rate 0.1 s^{-1}, pre-strain 0.4, deformation temperatures of 1100 °C and inter-pass time of 1 s, 10 s, 30 s and 100 s. (a) GB map at inter-pass time of 1 s, (b) LocMis map of (a), (c) GB map at inter-pass time of 10 s, (d) LocMis map of (c), (e) GB map at inter-pass time of 30 s, (f) LocMis map of (e), (g) GB map at inter-pass time of 100 s, (h) LocMis map of (g).

4. Conclusions

This paper studies the high temperature flow characteristics and SRX, MDRX softening behaviour of experimental steels under the interaction of deformation temperature, strain rate and pre-strain. The microstructure of the experimental steel after double-pass thermal compression is characterized to reveal the evolution law of the material microstructure under the influence of the thermal deformation parameters. Based on the 0.2% offset strain method, the softening rate of the experimental steel is determined under different deformation states, the effect of thermal deformation parameters on the SRX and MDRX volume fraction is obtained, and the kinetics of SRX and MDRX of the experimental steel is established. The main conclusions are obtained as follows :

(1) Based on the double-pass thermal compressive flow stress curves, it can be concluded that the experimental steel undergoes discontinuous yielding during deformation, and the second flow stress of SRX is significantly dependent on inter-pass time, deformation temperature, and strain rate. When pre-strain is 0.1 or 0.15, the flow stress changes less, and when pre-strain

increases to 0.2, the softening effect is enhanced. The second flow stress of MDRX significantly depends on inter-pass time, deformation temperature, and pre-strain has less effect on the second-pass flow stress.

(2) SRX needs time to nucleation, so softening effect of SRX is facilitated by a longer time between passes. MDRX is a dynamic recrystallization grain growth process and does not require a nucleation stage so that the material can be softened in a short time after deformation.

(3) The increase of inter-pass time, deformation temperature and strain rate can promote the SRX process and increase the static softening effect. Under the condition of constant deformation temperature, and strain rate, increasing pre-strain can increase the volume fraction of SRX. Compared with pre-strain, deformation temperature and strain rate have more pronounced effects on the static softening of the pass gap. The increase of inter-pass time, deformation temperature and strain rate can promote the MDRX process and increase the static softening effect, and compared with pre-strain, deformation temperature and strain rate have more obvious effects on the static softening of the inter-pass.

(4) The kinetic models of SRX and MDRX are established based on the experimental conditions. The model predictions and experimental values are compared well and could be used to predict the volume fraction of SRX and MDRX during the material deformation process. The thermal deformation activation energies of SRX and MDRX are 392.59 kJ/mol and 326.61 kJ/mol.

Declaration of Completing Interest

The authors declare that they have no known competing financial interests or personal relationships that could have appeared to influence the work reported in this paper.

Acknowledgments

REFERENCES

[1] Liu C, Peng Y, Barella S, Mapelli C, Liang S. Characterization of dynamic recrystallization behavior of low carbon steel under flexible rolling process. Mater Today Commun 2021;29:102777.

[2] Liu C, Mapelli C, Peng Y, Barella S, Liang S, Gruttadauria A, et al. Dynamic recrystallization behavior of low-carbon steel during the flexible rolling process: modeling and characterization. Steel Res Int 2022;93(4):2100490.

[3] Liu C, Barella S, Peng Y, Guo S, Liang S, Sun J, et al. Modeling and characterization of dynamic recrystallization under variable deformation states. Int J Mech Sci 2023;238:107838. https://doi.org/10.1016/j.ijmecsci.2022.107838. ISSN 0020-7403.

[4] Wang Q, Gao B, Wang K, Wang W, Tong L, Li X. Dynamic and static softening mechanisms of commercial-purity Zr during double-stage hot compressive deformation. Mater Sci Eng, A 2022;820:141578.

[5] Sakai T, Belyakov A, Kaibyshev R, Miura H, Jonas JJ. Dynamic and post-dynamic recrystallization under hot, cold and severe plastic deformation conditions. Prog Mater Sci 2014;60:130−207.

[6] Ding S, Khan S, Yanagimoto J. Metadynamic recrystallization behavior of 5083 aluminum alloy under double-pass compression and stress relaxation tests. Mater Sci Eng, A 2021;822:141673.

[7] Wang X, Chandrashekhara K, Buchely M, Lekakh S, Van Aken D, O'Malley R, et al. Experiment and simulation of static softening behavior of alloyed steel during round bar hot rolling. J Manuf Process 2020;52:281−8.

[8] Taylor A, Cizek P, Hodgson P. Comparison of 304 stainless steel and Ni−30wt.% Fe as potential model alloys to study the behaviour of austenite during thermomechanical processing. Acta Mater 2011;59(14):5832−44.

[9] Dong D, Chen F, Cui Z. Investigation on metadynamic recrystallization behavior in SA508-III steel during hot deformation. J Manuf Process 2017;29:18−28.

[10] Dong D, Chen F, Cui Z. Static recrystallization behavior of SA508-III steel during hot deformation. J Iron Steel Res 2016;23(5):466−74.

[11] Lin Y, Chen M, Zhong J. Study of metadynamic recrystallization behaviors in a low alloy steel. J Mater Process Technol 2009;209(5):2477−82.

[12] Zhou P, Ma Q. Static recrystallization behavior of 25CrMo4 mirror plate steel during two-pass hot deformation. J Iron Steel Res Int 2017;24(2):222−8.

[13] Shen W, Zhang C, Zhang L, Xu Q, Cui Y, Xu Y. A modified Avrami equation for kinetics of static recrystallization of Nb-V microalloyed steel: experiments and numerical simulation. Vacuum 2018;150:116−23.

[14] Lin Y, Fang X, Wang Y. Prediction of metadynamic softening in a multi-pass hot deformed low alloy steel using artificial neural network. J Mater Sci 2008;43(16):5508−15.

[15] Fernández A, Lopez B, Ibabe J. Relationship between the austenite recrystallized fraction and the softening measured from the interrupted torsion test technique. Scripta Mater 1999;40(5):543−9.

[16] Lin Y, Chen M, Zhong J. Static recrystallization behavior of deformed austenite in 42CrMo steel. Journal of Central South University (Medical Sciences); 2009. p. 411−6.

[17] Lin Y, Chen X, Chen M, Zhou Y, Wen D, He D. A new method to predict the metadynamic recrystallization behavior in a typical nickel-based superalloy. Appl Phys Mater Sci Process 2016;122(6).

[18] Lin Y, Li L, Xia Y. A new method to predict the metadynamic recrystallization behavior in 2124 aluminum alloy. Comput Mater Sci 2011;50(7):2038−43.

[19] Maghsoudi M, Zarei-Hanzaki A, Changizian P, Marandi A. Metadynamic recrystallization behavior of AZ61 magnesium alloy. Mater Des 2014;57:487−93.

[20] Razali M, Ghawi A, Irani M, Chung S, Choi J, Joun M. Practical approach for determining material parameters when

predicting grain size after static recrystallization. J Mater Res Technol 2023;23:3928—41.

[21] Sinha V, Payton EJ, Gonzales M, Abrahams RA, Song BS. Delineation of prior austenite grain boundaries in a low-alloy high-performance steel. Metallogr Microstruct Anal 2017;6(6):610—8.

[22] Thackray R, Palmiere EJ, Khalid O. Novel etching technique for delineation of prior-austenite grain boundaries in low, medium and high carbon steels. Materials 2020;13(15).

[23] Cho K, Sim H, Kim J, Choi J, Lee K, Yang H, et al. A novel etchant for revealing the prior austenite grain boundaries and matrix information in high alloy steels. Mater Char 2008;59(6):786—93.

[24] Bartolomé R, Jorge-Badiola D, Astiazarán J, Gutiérrez I. Flow stress behaviour, static recrystallisation and precipitation kinetics in a Nb-microalloyed steel after a strain reversal. Mater Sci Eng, A 2003;344:340—7.

[25] Zeng R, Huang L, Li J, Li H, Zhu H, Zhang X. Quantification of multiple softening processes occurring during multi-stage thermoforming of high-strength steel. Int J Plast 2019;120:64—87.

[26] Wang Z, Liu X, Xie F, Lai C, Li H, Zhang Q. Dynamic recrystallization behavior and critical strain of 51CrV4 high-strength spring steel during hot deformation. J Miner Met Mater Soc 2018;70:2385—91.

[27] Zhao M, Huang L, Zeng R, Wen D, Su H, Li J. In-situ observations and modeling of static recrystallization in 300M steel. Mater Sci Eng, A 2019;765:138300.

[28] Bo G, Jiang F, Su H, Wu L, Teng J, Fu D, et al. Static softening behavior and modeling of an Al—Cu—Mg—Zr alloy with various pre-precipitation microstructures during multistage hot deformation. Mater Sci Eng, A 2020;778:139094.

[29] Dehghan-Manshadi A, Barnett M, Hodgson P. Recrystallization in AISI 304 austenitic stainless steel during and after hot deformation. Mater Sci Eng, A 2008;485:664—72.

[30] Li X, Wu L, Chen J, Zhang H. Static softening characteristics and static recrystallization kinetics of aluminum alloy A6082 after hot deformation. J Shanghai Jiaot Univ 2010;15:307—12.

[31] Sun W, Hawbolt E. Comparison between static and metadynamic recrystallization-an application to the hot rolling of steels. ISIJ Int 1997;37(10):1000—9.

[32] Mao HJ, Zhang R, Hua L, Yin F. Study of static recrystallization behaviors of GCr15 steel under two-pass hot compression deformation. J Mater Eng Perform 2015;24:930—5.

[33] Jin Z, Yin K, Yan K, Wu D, Liu J, Cui Z. Finite element modelling on microstructure evolution during multi-pass hot compression for AZ31 alloys using incremental method. J Mater Sci Technol 2017;33(11):1255—62.

[34] Dong H, Cai D, Zhao Z, Wang Z, Wang Y, Yang Q, et al. Investigation on static softening behaviors of a low carbon steel under ferritic rolling condition. J Mater Eng Perform 2010;19:151—4.

[35] Qiao S, He X, Xie C, Liu Z. Static recrystallization behavior of SA508Gr.4N reactor pressure vessel steel during hot compressive deformation. J Iron Steel Res Int 2021;28(5):604—12.

[36] Elwazri A, Essadiqi E, Yue S. The kinetics of static recrystallization in microalloyed hypereutectoid steels. ISIJ Int 2004;44(1):162—70.

[37] Lin Y, Chen M. Study of microstructural evolution during metadynamic recrystallization in a low-alloy steel. Mater Sci Eng, A 2009;501(1):229—34.

[38] Chen F, Cui Z, Sui D, Fu B. Recrystallization of 30Cr2Ni4MoV ultra-super-critical rotor steel during hot dformation. Part III:

metadynamic recrystallization. Mater Sci Eng, A 2012;540:46—54.

[39] Chen M, Lin Y, Ma X. The kinetics of dynamic recrystallization of 42CrMo steel. Mater Sci Eng, A 2012;556:260—6.

[40] Zhao M, Huang L, Zeng R, Su H, Wen D, Li J. In-situ observations and modeling of metadynamic recrystallization in 300M steel. Mater Char 2020;159:109997.

[41] He D, Lin Y, Wang L. Microstructural variations and kinetic behaviors during metadynamic recrystallization in a nickel base superalloy with pre-precipitated δ phase. Mater Des 2019;165:107584.

[42] Li L, Zheng L, Ye B, Tong Z. Metadynamic and static recrystallization softening behavior of a bainite steel. Met Mater Int 2018;24:60—6.

[43] Taylor A, Hodgson P. The post-deformation recrystallization behaviour of 304 stainless steel following high strain rate deformation. Mater Sci Eng, A 2011;529:164—9.

[44] Liu J, Liu Y, Lin H, Li M. The metadynamic recrystallization in the two-stage isothermal compression of 300M steel. Mater Sci Eng, A 2013;565:126—31.

[45] Haghighat M, Sharma J, Gehrmann B, Alves H, Bozzolo N. Supersolvus recrystallization and grain growth kinetics for the fine tuning of grain size in VDM alloy 780 forgings. Metall Mater Trans 2023;54:2092—111.

[46] Ali M, Seppälä O, Fabritius T, Kömi J. Microstructure evolution and static recrystallization kinetics in hot-deformed austenite of coarse-grained Mo-free and Mo containing low-carbon CrNiMnB ultrahigh-strength steels. Mater Today Commun 2022;33:104676.

[47] Chen X, Tang B, Chen W, Yang Y, Zheng G, Fan Z, et al. Effect of inter-pass annealing on the deformation microstructure of Ti-48Al-2Cr-2Nb alloy. J Alloys Compd 2023;934:167751.

[48] Zhang H, Zhang K, Jiang S, Zhou H, Zhao C, Yang X. Dynamic recrystallization behavior of a γ′-hardened nickel-based superalloy during hot deformation. J Alloys Compd 2015;623:374—85.

Caiyi Liu is an assistant professor at School of Mechanical Engineering, Yanshan University, China. His research interests include materials characterization and mechanical properties during flexible rolling process.

Shicheng Liang is a PhD student at School of Mechanical Engineering, Yanshan University, China. His research interests include static recrystallization during flexible rolling process.

Shuo Guo is a PhD student at School of Mechanical Engineering, Yanshan University, China. His research interests include dynamic recrystallization during flexible rolling process.

Ruowei Li is a master's student at School of Mechanical Engineering, Yanshan University, China. His research interests include metadynamic recrystallization during flexible rolling process.

Silvia Barella is a professor at department of mechanical engineering, Politecnico di Milano, Italy. Her research interests solidification processes (casting and welding), hot and cold plastic deformation and the heat treatment of iron and aluminum based alloy.

Yan Peng is a professor at School of Mechanical Engineering, Yanshan University, China. His research interests include continuous strip rolling equipment-technology-product flexible adaptation and multi-objective synergistic control under instantaneous mutation.
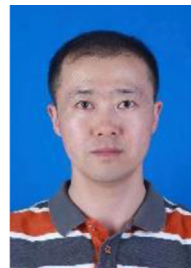
Andrea Gruttadauria is an associate professor at department of mechanical engineering, Politecnico di Milano, Italy. His research interests include solidification processes of metal alloys (casting and welding of ferrous and nickel-based alloys), plastic deformation and thermal treatments of iron-based alloys, nickel and aluminum.
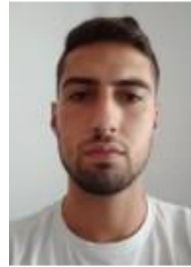
Marco Belfi is a PhD student at department of mechanical engineering, Politecnico di Milano, Italy. His research interests include heat treatment on the mechanical properties and microstructure of iron-based alloys, nickel and aluminum.

Wei Li is an engineer at WISDRI Engineering & Research Incorporation Limited, China. His research interests centering on fundamental and application fields, such as lightweight steel material, metallurgical process and equipment, microstructure characterization and performance evaluation.

Chang Yuan is a bachelor's student at School of Mathematics, University of Bristol, UK. Her research interests include applying engineering mathematics principles for material constitutive modeling.

Carlo Mapelli is a professor at department of mechanical engineering, Politecnico di Milano, Italy. His research interests include thermodynamics and kinetics of steel and metallurgical processes.